

A Lagrangian Model-Based Analysis of Protist Plankton Variability and Its Impact on Organic Matter Dynamics Along Transit Pathways Through the Fram Strait

Vanessa Lampe¹ , Aidan Hunter² , Ben Andrew Ward³ , Eva-Maria Nöthig⁴, Anja Engel¹ , Ingrid Helene Ellingsen⁵, and Markus Schartau¹ 

¹GEOMAR Helmholtz Centre for Ocean Research, Kiel, Germany, ²British Antarctic Survey, Cambridge, UK, ³University of Southampton, Southampton, UK, ⁴Alfred Wegener Institute, Helmholtz-Centre for Polar and Marine Research, Bremerhaven, Germany, ⁵SINTEF Ocean, Trondheim, Norway

Key Points:

- Local variability in tracer concentrations in Fram Strait (FS)'s upper 100 m is linked to differences in water parcel trajectories
- Trajectories differ in their origin and timing of passage, leading to differences in plankton size structure, growth, and export
- At the time of in situ observations in the FS, the maxima in net primary production and vertical export have already occurred

Supporting Information:

Supporting Information may be found in the online version of this article.

Correspondence to:

V. Lampe,
vlampe@geomar.de

Citation:

Lampe, V., Hunter, A., Ward, B. A., Nöthig, E.-M., Engel, A., Ellingsen, I. H., & Schartau, M. (2024). A Lagrangian model-based analysis of protist plankton variability and its impact on organic matter dynamics along transit pathways through the Fram Strait. *Journal of Geophysical Research: Oceans*, 129, e2024JC021254. <https://doi.org/10.1029/2024JC021254>

Received 23 APR 2024

Accepted 26 SEP 2024

Corrected 24 OCT 2024 and 18 NOV 2024

This article was corrected on 24 OCT 2024 and 18 NOV 2024. See the end of the full text for details.

Author Contributions:

Conceptualization: Vanessa Lampe, Markus Schartau

Data curation: Aidan Hunter, Eva-Maria Nöthig, Anja Engel, Ingrid Helene Ellingsen

Formal analysis: Vanessa Lampe

Funding acquisition: Ben Andrew Ward, Anja Engel, Markus Schartau

Investigation: Vanessa Lampe

Abstract The Arctic Ocean is characterized by substantial seasonal and inter-annual variability, of which the sources and impacts are not yet fully understood. Here, we analyze how much of the variability found in in situ observations of biogeochemical and ecological variables collected at the Long-Term Ecological Research Observatory HAUSGARTEN can be explained by differences in the physical conditions in the water masses passing through the Fram Strait (FS). Employing a size-based plankton ecosystem model with nine distinct size classes of protist phyto- and zooplankton, we simulate standing stocks and fluxes within the nutrient, phytoplankton, zooplankton, and detritus pools in water parcels that follow trajectories tracing the opposing East-Greenland and West-Spitsbergen currents through the FS. Our model results agree with in situ observations of biogeochemical tracers, plankton size measurements, climatological data, and remote sensing observations. They show distinct temporal developments in plankton size composition, growth, and export in trajectory ensembles, highlighting how variable physical conditions affect the communities' specific growth histories. Our study indicates that 10%–72% of the variability in upper water column tracer concentrations observed in the FS can be attributed to differences in water parcel trajectories. The maxima of net primary production and vertical export along the trajectories occurred in some (spatial and temporal) distance upstream of the sites of in situ sampling. This study shows that Lagrangian modeling helps clarify complex biogeochemical-ecological relationships in highly dynamic systems such as the FS, which is urgently needed to understand the role of climate change in the Arctic carbon cycle.

Plain Language Summary To study sources of biological and chemical variability in the Fram Strait (FS) (Arctic Ocean), this study uses a model that follows water parcels as they move along the currents and simulates the growth of plankton populations, their influence on nutrient concentrations and the production of dead, dissolved, and decaying organic matter. By simulating many different pathways, the model estimates how variability in the environmental conditions along those pathways contributes to the variability of the plankton ecosystem in the upper water column. When compared to real data measured from ships and observed by satellites, we find that the model successfully reproduces changes in the plankton size structure and estimates productivity and export close to observations from the region. Our study finds that a substantial portion (10%–72%) of the observed variability in biogeochemical tracers can be explained by differences in the origins and pathways of water parcels. Nonetheless, a large amount of variability remains unexplained, indicating the need for further research to better understand essential processes. This research helps us understand the sources of variability in the FS and make better predictions about elemental cycling, productivity and export, which is especially important in the face of climate change.

1. Introduction

The Arctic Ocean has changed significantly in recent decades as sea surface temperatures have risen (Comiso & Hall, 2014; Nielsen-Englyst et al., 2023) and the extent and thickness of sea ice has declined (E. Hansen et al., 2013; Renner et al., 2014; Spreen et al., 2020; Stroeve et al., 2012). These changes in the environment may substantially modify biogeochemical processes and alter the functioning of marine ecosystems.

The Fram Strait (FS), between Greenland and Spitsbergen, is one of the main gateways to the Arctic Ocean and has been the subject of numerous repeated studies in the fields of biological, chemical and physical oceanography.

© 2024. The Author(s).

This is an open access article under the terms of the [Creative Commons Attribution License](https://creativecommons.org/licenses/by/4.0/), which permits use, distribution and reproduction in any medium, provided the original work is properly cited.

Methodology: Vanessa Lampe, Aidan Hunter, Markus Schartau
Project administration: Markus Schartau
Resources: Ben Andrew Ward, Eva-Maria Nöthig, Anja Engel, Ingrid Helene Ellingsen, Markus Schartau
Software: Vanessa Lampe, Aidan Hunter, Ben Andrew Ward, Markus Schartau
Supervision: Ben Andrew Ward, Markus Schartau
Validation: Vanessa Lampe, Aidan Hunter, Ben Andrew Ward, Markus Schartau
Visualization: Vanessa Lampe
Writing – original draft: Vanessa Lampe
Writing – review & editing: Vanessa Lampe, Aidan Hunter, Ben Andrew Ward, Eva-Maria Nöthig, Anja Engel, Ingrid Helene Ellingsen, Markus Schartau

A target area in the FS covers the Long-Term Ecological Research (LTER) observatory HAUSGARTEN (e.g., Soltwedel et al., 2005, 2016), where warmer waters enter from the North Atlantic in the East (West-Spitsbergen current, WSC) and colder, seasonally ice-covered waters exit the Arctic Ocean southwards in the West (East-Greenland Current, EGC). With the WSC and the EGC passing through the HAUSGARTEN area, the observations at different sampling sites capture biological and chemical signals that are influenced by dynamical changes that have already taken place outside the study area, for which data with comparable details are not available.

Most in situ investigations conducted in the FS have focused on the summer conditions (e.g., Nöthig et al., 2020), as the region is seasonally covered with sea ice or close to the ice edge. More recent studies also covered periods in autumn or spring (e.g., von Jackowski et al., 2020a, 2022). Observations from the dark winter months are still rare (e.g., Błachowiak-Samołyk et al., 2015; Wietz et al., 2021). Detecting longer-term trends from annually repeated observations in summer and autumn within the FS is difficult given the strong spatial and temporal variability in ice cover and hydrographic conditions and usually requires many years, if not decades, of data collection. Helpful in this respect is to disentangle the range and causes of the observed variability within such regions, which contributes to our understanding of the processes involved. Thus, the motivation for this modeling study is to resolve the impact of variable environmental conditions on the variability of biogeochemical variables across regions connected by water mass transport.

In principle, variability in organic matter (OM) observations is conditioned by a combination of external factors, which are variations in physical and chemical conditions such as light, nutrient availability, and temperature, as well as of internal factors that are associated with the plankton dynamics. Overall, in the context of this study, we are concerned with different sources of variability that are linked to each other and become ultimately expressed in regions of observations:

- I. Spatio-temporal variations in environmental conditions
 - differences in the horizontal transport of water masses (pathways)
 - differences in vertical mixing
- II. Temporal variations in plankton dynamics
 - differences in plankton physiology, community structure, and interaction
 - differences in pre-conditioning, spatial origin and growth history of the plankton community

Apart from purely stochastically driven (random) processes, and disregarding methodological uncertainties, individual in situ measurements are subject to these major sources of variability that create differences between nearby but distinct sampling sites. For example, the diversity of plankton is shaped by their dispersion and advection across environmental gradients (Barton et al., 2010; Lévy et al., 2014), responsible for much of the variability observed within a particular region. On regional scale, variability and differences in characteristic timescales of phytoplankton are expected to be better represented in a Lagrangian framework (Kuhn et al., 2019), since mechanisms that drive local bio-physical dynamics can be effectively described along the actual landscape of a drifting and evolving ecosystem (Ser-Giacomi et al., 2023). Furthermore, a difficulty in ecosystem modeling is the identification of appropriate model parameters for an area of interest, which is complicated by the commonly used Eulerian perspective, but is facilitated by accounting for the evolution of nutrients and plankton along advection pathways explicitly (Kida & Ito, 2017).

The horizontal heterogeneity observed during a limited period of ship-board sampling (usually 2–3 weeks) in the HAUSGARTEN can, to some extent, be attributed to differences in the prior history along different pathways of water parcels passing through that region. These pathways can be investigated with a Lagrangian modeling approach, allowing dynamically consistent solutions of a one-dimensional (1D) marine ecosystem model to be derived along trajectories of individual water parcels (e.g., Banas et al., 2009). This approach facilitates the identification of optimized model solutions due to its computational efficiency (Banas, Zhang, et al., 2016), as model calibration requires multiple simulation runs. In a recent global comparison study by Kuhn et al. (2023) it is shown that the variability in Chl-*a* concentration is similarly described by an Eulerian and a Lagrangian approach on timescales of 30 days (approximately two times the characteristic timescale of plankton growth). Only in some ocean areas, with boundary currents or in upwelling regions, can differences between the two approaches become significant. With regard to plankton ecosystems in ocean regions that include frontal systems like in the FS, the findings of Kuhn et al. (2023) suggest suitable descriptions when a Lagrangian perspective is chosen. To investigate the spatial heterogeneity found in the HAUSGARTEN data the Lagrangian approach is particularly useful, as

it allows us to connect detailed local observations, for example, plankton community structure, to spatio-temporal variations in tracer concentrations, primary production and carbon export outside of the target region.

Many aspects of plankton dynamics, from cellular to community level, are controlled by cell size, which can be regarded as a “master trait” (Andersen et al., 2016; Blanchard et al., 2017; Marañón, 2015). Physiological processes such as nutrient assimilation and photosynthetic rates are size dependent (e.g., Edwards et al., 2012; Litchman et al., 2007), as are predator-prey interactions (e.g., B. Hansen et al., 1994). Size based ecosystem models make use of these allometric features to explain structural changes of the plankton community (e.g., Banas, 2011; Moloney & Field, 1991; Ward & Follows, 2016; Ward et al., 2012). Litchman et al. (2007) have shown that trade-offs between ecophysiological and morphological traits arise from fundamental allometric relationships that describe diverse plankton interactions and can explain variations in community composition along environmental gradients. Similarly, Ward et al. (2012) have shown that their size-structured ecosystem model was able to reproduce global patterns in biogeography and community structure of marine plankton, demonstrating the utility of size-based modeling.

Our primary objective is to investigate to what extent the differences between the environmental conditions (histories) of horizontally advected water parcels (trajectories) may contribute to the spatial heterogeneity of particulate and dissolved organic matter (POM and DOM) concentrations in the FS, as observed during summer and autumn of 2018 respectively. Along four ensembles of Lagrangian trajectories, which differ with respect to their origins and times passing the observational HAUSGARTEN area in the FS, a 1D size-based plankton ecosystem model is applied. We assess the model's ability to reproduce changes in the community size spectra observed in Lampe et al. (2021), where the plankton community showed a shift toward larger cell size during the summer-autumn transition in 2018. We provide insight into the differences in simulated rates of NPP and export, and explicitly resolve stoichiometric variations in carbon-to-nitrogen and Chl-*a*-to-carbon ratios before, during, and after the sampling periods along trajectories that originate from either the Arctic to the north or the North Atlantic regions to the south.

2. Methods

This study follows a Lagrangian approach, where we apply a one-dimensional (1D, vertically resolved) ecosystem model and force it with data of the physical environment along transport pathways (trajectories) through the FS. The ecosystem model is a size structured nutrient-phytoplankton-zooplankton-detritus (NPZD) model with nine size classes for phytoplankton and zooplankton. Some model parameters important for physiology and ecological interactions (e.g., regulating cell quota, nutrient uptake, growth, mortality, and grazing) are dependent on organism size and scale allometrically with cell volume. The oceanographic conditions that force the plankton model were extracted from SINMOD model results (Slagstad & McClimans, 2005; Wassmann et al., 2006) along trajectories passing the HAUSGARTEN site in the FS. Four ensembles of trajectories that differ in their origin (North Atlantic vs. northern FS) and timing of passage (summer vs. autumn) allow us to obtain multiple model solutions (see Section 2.2). For model calibration we use observational data collected in the FS, which comprise tracer concentration measurements (Engel et al., 2019; Torres-Valdés et al., 2019; von Jackowski et al., 2020b) as well as microscopic measurements of cell abundance and cell size (Lampe et al., 2021). We fit the model to observations (in situ, remote sensing, and climatological data) by adjusting the model parameters. In addition, remote sensing Chl-*a* data (Sathyendranath et al., 2021), and climatological data of the World Ocean Atlas 2018 (WOA18, Boyer et al., 2018) are considered for model evaluation.

2.1. Observational Data

In situ observational data were collected at the HAUSGARTEN LTER observatory site in the FS, located between Greenland and Spitsbergen (see Figure 1). This region is commonly referred to as a main gateway to the Arctic Ocean (e.g., Nöthig et al., 2015) and is characterized by the convergence of two hydrographic regimes. While the eastern part of the FS is dominated by the northward flowing West-Spitsbergen-Current (WSC) that transports warm water from the North Atlantic into the Arctic Ocean (e.g., Beszczynska-Möller et al., 2012), the East-Greenland-Current (EGC) carries cold Arctic water into the Atlantic through the western FS (e.g., de Steur et al., 2009). The western region of the FS remains covered with sea ice for most of the year. More seasonal variability in sea ice cover is observed in the north-eastern, WSC dominated, part while the south-eastern region stays ice free throughout the year (Soltwedel et al., 2016). The HAUSGARTEN LTER is located in the central FS

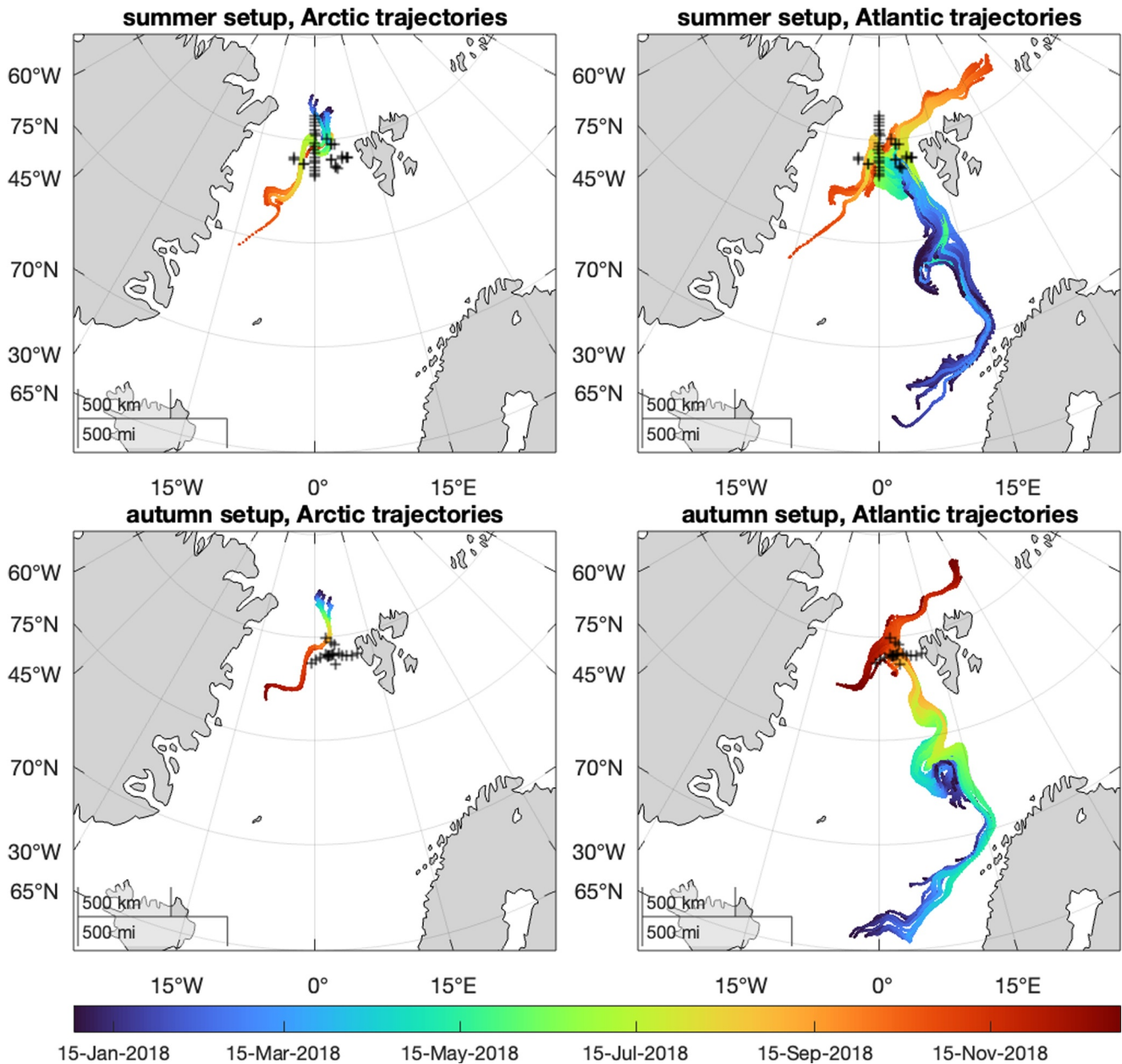


Figure 1. Ensembles of particle trajectories for the physical model forcing. The color scales indicates the dates at each location. The starting point at day = 1 is indicated in dark blue (in the Northern Fram Strait, Arctic origin, left panels; or in the Norwegian Sea, Atlantic origin, right panels). Black crosses mark the HAUSGARTEN sampling stations of observational in situ data used for model evaluation. Trajectories of the summer setup pass the stations during the summer sampling period (16 July–27 July 2018), those of the autumn setup during the autumn sampling period (16 September–4 October 2018).

between 78°N and 81°N and 5°W–11°E and includes sampling stations in the colder EGC waters, as well as in the warmer WSC waters. The Marginal Ice Zone is a highly productive region (Soltwedel et al., 2016).

The data consist of in situ concentration measurements of inorganic nitrogen (nitrite and nitrate) (Torres-Valdés et al., 2019), and chlorophyll-*a* (Chl-*a*), particulate organic carbon (POC) and nitrogen (PON) (Engel et al., 2019; von Jackowski et al., 2020b), collected between 16 July and 27 July 2018 during the PS114 expedition of research vessel RV *Polarstern*. Additionally to the observational data recorded during summer time, we also consider data from a research cruise in autumn. Autumn samples were collected on MSM77 research cruise on RV *Maria S. Merian* between 16 September and 4 October 2018 and include measurements of Chl-*a* and POC. Unfortunately, no measurements of dissolved inorganic nitrogen (DIN) and PON were conducted during this expedition. To

Table 1

Model Parameters: The First 17 Parameters Are Independent of Cell Size, While the Remaining Seven Parameters Are Described According to an Allometric Relationship ($x = a \cdot (\frac{Vol}{1 \mu m^3})^b$)

(#) Notation	Values	Unit	Description (equation)
(1) T^{ref}	20	°C	Reference temperature (Equation S5 in Supporting Information S1)
(2) A	0.05	–	Temperature sensitivity (Equation S5 in Supporting Information S1)
(3) h	10	–	Uptake quota regulation (Equation S4 in Supporting Information S1)
(4) m_2	0.05 ^a	m ³ mmol C ⁻¹ d ⁻¹	Quadratic mortality (Equation S24 in Supporting Information S1)
(5) a_p^*	3.83 · 10 ⁻⁷	mol C m ⁻² (g Chl <i>a</i> μEin) ⁻¹	Initial slope of P-I curve (Equations S8 and S14 in Supporting Information S1)
(6) θ	4.2	mg Chl- <i>a</i> :N (mmol N) ⁻¹	Maximum Chl- <i>a</i> :N ratio (Equation S14 in Supporting Information S1)
(7) ξ	2.33	mol C (mol N) ⁻¹	Cost of biosynthesis (Equation S12 in Supporting Information S1)
(8) a_G^b	4	m ³ (day mmol C) ⁻¹	Grazing clearance rate (Equation S16 in Supporting Information S1)
(9) k_G	2.75	mmol C (m ³) ⁻¹	Total prey half saturation (Equations S15 and 16 in Supporting Information S1)
(10) δ_{opt}	10	–	Optimum predator-prey size ratio (Equation S18 in Supporting Information S1)
(11) σ^b	2	–	Width of grazing kernel (Equation S18 in Supporting Information S1)
(12) Λ	–1	–	Prey refuge parameter (Equation S15 in Supporting Information S1)
(13) λ^{max}	0.7	–	Max. assimilation efficiency (Equations S21 and 22 in Supporting Information S1)
(14) m_{min}	0.01	d ⁻¹	Summand to prevent m_j approaching 0 (Equation S23 in Supporting Information S1)
(15) $r_{i,k}^b$	0.04	d ⁻¹	Remineralization rate (Equations 1 and 3)
(16) β	$b_1 = 0.9, b_2 = 0.2222, b_3 = 2$	–	Detritus and DOM partitioning (Equations S25–S27 in Supporting Information S1)
(17) w_{det}^b	10	m d ⁻¹	Sinking velocity of detritus (3)
	$(x = a \cdot Vol^b)$	(Unit of x)	
(18) Q_N^{min}	$a^b = 0.035, b = 0$	mol N (mol C) ⁻¹	Minimum N:C quota (Equations S2–S4 in Supporting Information S1)
(19) m	$a^b = 0.05, b = 0$	d ⁻¹	Mortality rate (Equation 2; Equation S23–S27 in Supporting Information S1)
(20) \bar{s}_N^{max}	$a^b = 0.6166, b^b = -0.09$	–	Scaling of maximum N:C quota (Equation S2 in Supporting Information S1)
(21) v^{max}	$a^b = 0.1008, b^b = 0.09$	mol N (mol C) ⁻¹ d ⁻¹	Maximum uptake rate (Equation S6 in Supporting Information S1)
(22) α	$a^b = 0.5933, b^b = -0.18$	m ³ (mmol C) ⁻¹ d ⁻¹	Nutrient affinity (Equation S6 in Supporting Information S1)
(23) P^{max}	$a^b = 2.5, b^b = -0.08$	d ⁻¹	Maximum photosynthetic rate (Equation S7 in Supporting Information S1)
(24) G^{max}	$a^b = 11, b^b = -0.16$	d ⁻¹	Maximum prey capture rate (Equations S15 and S16 in Supporting Information S1)

Note. Two of the originally assumed size-dependent parameters (Q_N^{min} and m) yielded the best fit when assigned no size dependency (i.e., $b = 0$). ^aFor the largest size class, otherwise 0. ^bParameter was considered in numerical optimization, see Section 2.4.

complement the biogeochemical tracers, we also considered ecological data to evaluate the model. For this, we used plankton size data in the form of size spectra of the protist plankton community, as described in Lampe et al. (2021), where size spectra of 60 samples from summer (PS99, PS107, PS114) and autumn (MSM77) and both the WSC and ESC influenced HAUSGARTEN stations were used.

2.2. Model Setup and Forcing

The 1D-NPZD model resolves $n = 9$ size classes of phytoplankton and zooplankton with variable stoichiometry (carbon-to-nitrogen, C:N ratio), similar to the size-based models of Ward et al. (2012) and Ward and Follows (2016). In this model, 10 important parameters controlling the physiology (e.g., nutrient uptake rates, biosynthesis rates) and ecology (e.g., grazing) are dependent on organism size (see Table 1). We chose a Lagrangian approach to simulate lateral dispersal of the plankton along with the water currents (flow field). Along these trajectories the plankton experience changing environmental conditions, including variations in vertical mixing and exposure to light. The target region is the HAUSGARTEN observatory in the FS, to be reached at times that cover the two sampling periods, in summer and autumn.

2.2.1. Physical Forcing

The physical forcing data were extracted from the ocean model SINMOD (Slagstad & McClimans, 2005; Wassmann et al., 2006), a regional coupled 3D model system encompassing physical, chemical, and biological domains. Configured for the Nordic and Arctic Seas, it operates at a horizontal resolution of 20 km and with 25 vertical layers. The hydrodynamic component, responsible for calculating fundamental oceanic properties such as velocity, water temperature, and pressure, is based on the primitive Navier-Stokes equations, implemented on a z -grid (Slagstad & McClimans, 2005; Slagstad et al., 2015). The ice model incorporates two state variables: ice thickness and concentration, shaping ice interaction dynamics (Hibler, 1979). This model integrates the ice momentum equation and an equation for ice internal stress, utilizing the elastic-viscous-plastic (EVP) dynamical model proposed by Hunke and Dukowicz (1997). Vertical turbulent diffusivity is calculated based on a Richardson number based scheme described in Sundfjord et al. (2008). Surface irradiance is calculated based on solar elevation, cloud cover and light attenuation through sea ice. Cloud cover is obtained from ERA-Interim reanalysis data from the ECMWF (European Center for Medium-Range Weather Forecasts). Details regarding the model runs including atmospheric, freshwater and tidal forcing utilized in this study can be found in Vernet et al. (2021). The data extraction was achieved by applying the *particulator* MatLab tool (Banas, 2018). The extracted data include surface irradiance ($I_{\text{surf}}(t)$), water temperature ($T(z,t)$) and vertical (turbulent) diffusivity ($K(z,t)$) for times t (day) and depths z (m). The spatio-temporal development of $I_{\text{surf}}(t)$ and surface temperature are shown in Figure 2. Irradiance attenuates exponentially with depth ($I(z,t)$), assuming a seawater attenuation coefficient of $\kappa_{\text{SW}} = 0.04 \text{ m}^{-1}$ (Lorenzen, 1972) together with a light attenuation by Chl-*a*, which is $\kappa_{\text{P}} = 0.0149 \text{ m}^2 (\text{mg Chl})^{-1}$ (Krause-Jensen & Sand-Jensen, 1998), see Equations S10 and S11 in Supporting Information S1. The pathways of these model trajectories are shown in Figure 1.

The model is applied in two seasonal setups, both of which distinguish between trajectories of Arctic and Atlantic origin. In the first “summer” setup, we isolated particle trajectories that passed through the HAUSGARTEN region during the July 2018 sampling period by defining “catchment areas” at the location of each in situ sample. Trajectories within 25 km from a sample location at the time of sampling were retained, and all other trajectories passing through FS were omitted. The radius of 25 km was selected after considering several factors, including the proximity of neighboring HG stations, the geographical context, and the availability of trajectories. The distances between the stations sampled in 2018 range from 10 to 20 km and the FS is approximately 500 km wide at HAUSGARTEN. A 25 km radius therefore ensures that the trajectories pass in reasonable proximity to the stations and capture the local variability without averaging over a too broad area. Finally, the radius must be large enough so that sufficient trajectories are included to provide a robust representation of the physical forcing (based on SINMOD 20 km spatial model grid resolution). A too small radius may lead to the exclusion of some stations, because then too few trajectories cross within the defined proximity. Eddies in this region are typically smaller than 20 km, with an average radius of 5 km (Wekerle et al., 2020), therefore these small-scale features are not properly resolved. Observational samples were usually taken in regions with no or thin ice cover. We therefore excluded trajectories of Arctic origin with high ice cover (ice cover > 50% in July) from the pool of forcing trajectories. In total, 139 trajectories of Atlantic origin and 10 trajectories of Arctic origin have been applied to force the model in the summer setup.

In the second “autumn” setup, we focused on trajectories passing through the HAUSGARTEN region during the September to October 2018 sampling period. To reach the target region later in the year, Atlantic-origin trajectories began further south, and Arctic-origin began further north than in the summer setup. Due to the limited number of available SINMOD particle trajectories and sampling stations from the field campaigns, the catchment area for trajectories had to be increased to a 100 km radius around the HAUSGARTEN stations for this setup. With a 25 km catchment area radius like in the summer setup, no trajectories of Arctic origin would remain for the autumn setup. Ultimately, five trajectories of Arctic origin and 50 of Atlantic origin were considered for the autumn setups.

2.2.2. Plankton Ecosystem Dynamics

The dynamical plankton ecosystem model is described by a set of differential equations that describe the mass flux of nitrogen and carbon. The phytoplankton and zooplankton are structured according to cell size (9 size classes: 1.12–2.00; 2.00–3.56; 3.56–6.33; 6.33–11.25; 11.25–20.00; 20.00–35.57; 35.57–63.25; 63.25–112.48; 112.48–200 μm equivalent spherical diameter, ESD), applying allometric rates that determine autotrophic growth within the respective size classes, as well as size-specific grazing by heterotrophs. While some parameters are

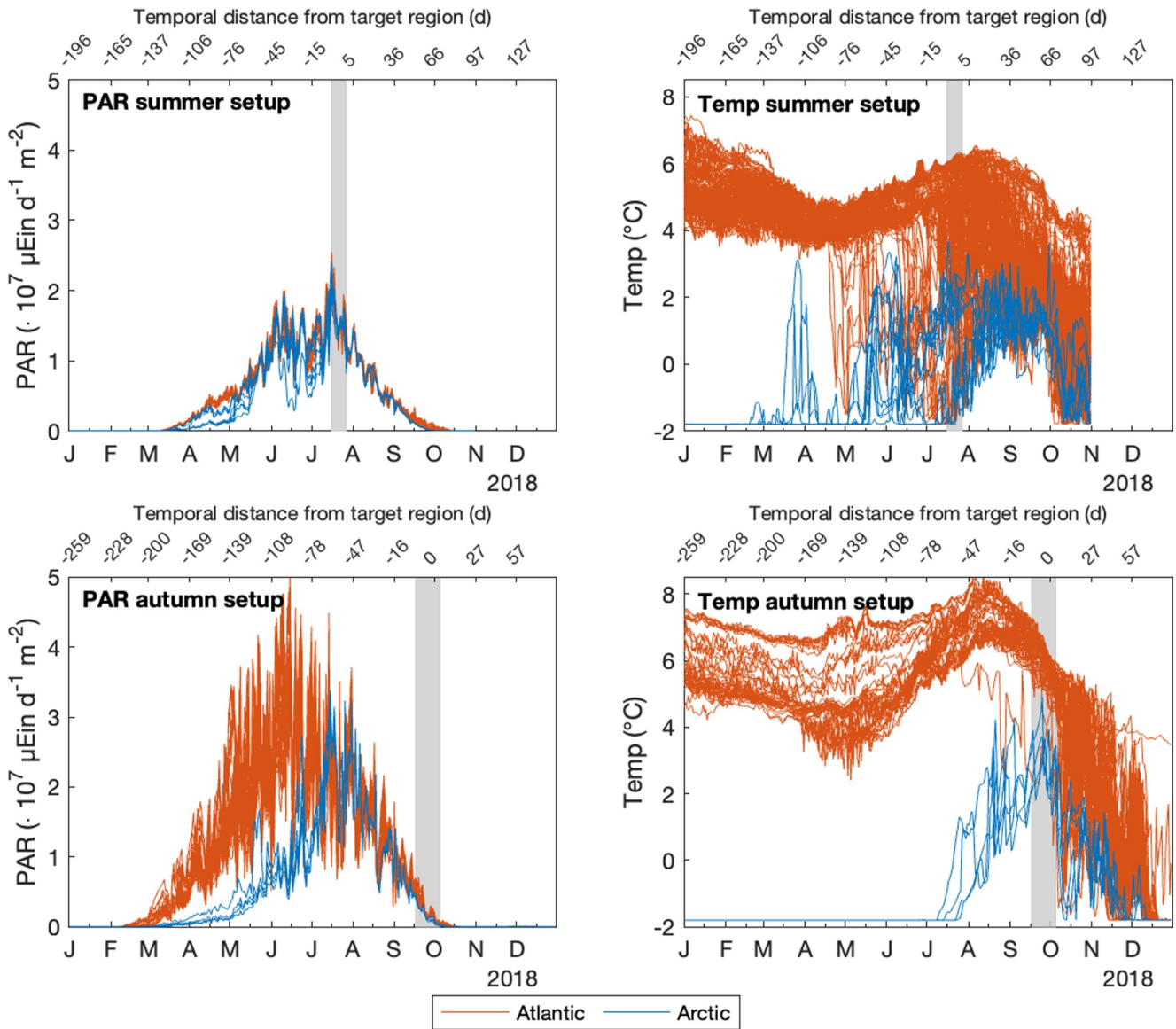


Figure 2. Physical conditions along the simulated model trajectories. The left column shows the history of surface PAR ($= I_{\text{surf}}(t)$) for the summer (upper) and autumn (lower) setup, the right column shows the history of sea surface temperature. Line colors indicate the trajectory origins (Arctic = blue or Atlantic = orange). Gray shaded areas exhibit the periods trajectories pass the HAUSGARTEN stations. In situ sampling was conducted between 16 July to 27 July 2018 and 16 September to 4 October 2018.

independent of organism size, others are dependent on the cell size, for example, maximum cell nutrient quota, nutrient uptake, and linear mortality. The model's parameter values are listed in Table 1. The differential equations are adapted from Ward et al. (2012, 2017), but modified to represent a 1D water column and with some minor changes to parameterization:

$$\frac{\partial N}{\partial t} = \frac{\partial}{\partial z} K \frac{\partial N}{\partial z} - \sum_j V_{N,j} B_{C,j} + \sum_k r_{N,k} M_{N,k} \quad (1)$$

$$\begin{aligned} \frac{\partial B_{i,j}}{\partial t} = & \frac{\partial}{\partial z} K \frac{\partial B_{i,j}}{\partial z} + V_{i,j} B_{C,j} - \sum_{j_z} G_{i,j_z} B_{C,j_z} \\ & + \sum_j \lambda_{i,j_z} G_{i,j_z} B_{C,j_z} - (m_j + m_2 B_{i,j}) B_{i,j} \end{aligned} \quad (2)$$

$$\frac{\partial D_{i,k}}{\partial t} = \frac{\partial}{\partial z} K \frac{\partial D_{i,k}}{\partial z} - w_k \frac{\partial D_{i,k}}{\partial z} - r_{i,k} D_{i,k} + \sum_j \beta_{j,k} (m_j + m_2 B_{i,j}) B_{i,j} + \sum_{j_z} B_{C,j_z} \sum_j \beta_{j,k} (1 - \lambda_{i,j_z}) G_{i,j_z,j} \quad (3)$$

Here, the state variables are concentrations of N (DIN), $B_{i,j}$ (phytoplankton and zooplankton biomass, a stacked matrix $B_{i,j} = [P_{i,j_p}, Z_{i,j_z}]$) and $D_{i,k}$ (dissolved and detrital particulate OM, DOM, and detritus respectively). Subscripts index biomass components ($i \in C, N, \text{Chl-}a$), plankton size classes ($j = [j_p, j_z] \in 1, \dots, n_p + n_z$), and type of detrital OM ($k \in \text{DOM, detritus}$). Chlorophyll is relevant only for phytoplankton, so the zooplankton and OM matrix rows where $i = \text{Chl-}a$ are zeroed.

The rate of change in DIN is the sum of changes due to vertical mixing and replenishment via remineralization minus the uptake by autotrophs. The rate of change in biomass is the sum of changes due to vertical mixing, autotrophic uptake (phytoplankton), uptake through grazing (zooplankton) minus changes due to grazing and mortality. The rate of change in D (DOM and detrital, particulate OM) is the sum of changes due to vertical mixing, mortality and sloppy feeding minus sinking and remineralization. Because the model only resolves the labile-semi-labile fraction of DOC, we refer to it as DOC_{SL} . The detailed terms of model Equations S1–S3 are described in Text S1 in Supporting Information S1.

The efficiency at which the primary production is exported to depth is diagnosed from the model results as the pe-ratio, and is calculated as the ratio of the total export flux at 100 m (combining the sinking of detritus ($w_{\text{det}} \cdot [D_{i,\text{POM}}]_z$) and the net flux induced from the turbulent vertical diffusion of POM (detritus + zooplankton + phytoplankton)) to the depth-integrated (100 m) NPP (e.g., Le Moigne et al., 2015; Serra-Pompei et al., 2022). The pe-ratio is therefore calculated as:

$$pe = \frac{\text{export}}{\text{NPP}} \quad (4)$$

In this study, we considered instant, daily pe-ratios and time integrated pe-ratios over the productive period. For the time integrated pe-ratios, we integrated export and NPP over April–September prior to calculation of the ratios.

2.2.3. Initial Conditions

The initial conditions were largely adopted from SINMOD simulation results. With regard to initial DIN profiles (at the origins on 1 January) of the Arctic trajectories, the SINMOD results exhibit surface concentrations around 6–7 mmol m^{-3} , which are lower than those derived in the WOA18 (10–11 mmol m^{-3}). For these Arctic trajectories we therefore adjusted the initial conditions to agree with the profiles of the WOA18 data by increasing the initial concentrations from 6–7 to 10–11 mmol m^{-3} . Plankton N biomass was initialized by splitting SINMOD's small and large phytoplankton N biomass evenly across the respective model size classes. For the initial plankton C biomass a constant C:N factor of 6.625 is imposed. We assume Chl- a :N at 75% of the maximum Chl- a :N ratio to be reasonable for model initialization on Jan 1st, and therefore calculated initial Chl- a biomass as $B_{\text{Chl},j_p} = 0.75 \cdot B_{\text{N},j_p} \cdot \theta$, with θ being the maximum Chl- a :N ratio (Table 1).

Initial detritus was derived from initial plankton. We assume that detrital OM equals a small fraction of plankton OM, and therefore derive $\sum_k M_{i,k} = 0.05 * \sum_j B_{i,j}$. Of the total detrital OM, $\sum_k M_{i,k}$, half is assumed dissolved, and the other half particulate. We stress that the sensitivity of the simulated phytoplankton and zooplankton biomass in spring, summer and autumn to variations of the initial conditions turned out to be extremely small. This is because of the prolonged period of darkness during the first months of the year; long enough to cause respective biomass to converge toward negligible concentrations in the range of $1 \cdot 10^{-8} \text{ mmol C m}^{-3}$, which is given after approximately 40 days.

2.3. Model Assessment

Monthly mean climatological DIN concentrations of WOA18 (Boyer et al., 2018; Garcia et al., 2019) are considered for evaluating the model's performance with regard to spatio-temporal changes in nutrient acquisition

along the pathways of the trajectories. On local scales, the ensembles of model solutions are assessed against the in situ measured DIN, Chl-*a*, POC, and PON concentrations of the respective sampling periods in the FS. The corresponding biovolume-size spectra derived from microscopic measurements are considered for an evaluation of the size-specific structural changes resolved by the model. In principle two different metrics are applied, the Root Mean Square Deviation (RMSD) for the tracer concentrations and a divergence function for the plankton size spectra.

2.3.1. Root Mean Square Deviation and Coefficient of Variation

In order to quantify the model's ability to reproduce the in situ observational data collected during the cruises, we calculated the RMSD for DIN (nitrate + nitrite), Chl-*a*, POC, and PON. We deliberately choose the notation RMSD instead of Root Mean Square Error, as it is not exclusively a model error, but also includes the variation between individual model trajectories. Accordingly, a wide spread of solutions of all trajectories will yield a RMSD that is higher than for cases where these solutions are very similar.

$$\text{RMSD} = \sqrt{\frac{1}{N} \sum_p^{n_p} \sum_t^{n_t} \sum_z^{n_z} (\text{mod}_{p,t,z} - \text{obs}_z^*)^2} \quad (5)$$

Here, $\text{obs}_z^* = \text{median}(\text{obs})_z$ is the median of all individual samples at depth z across all days and $N = n_p + n_t + n_z$. The indices represent model trajectory (p), day-of-year (Julian day) (t), and depth (z). Model results were interpolated to depths where data are available. For the calculation of RMSD, we distinguish between trajectories according to their origins (Arctic and Atlantic) for both model setups (summer and autumn).

Furthermore, we derived a measure that relates the RMSD to the corresponding mean of obs_z^* , similar to a coefficient of variation (CV):

$$\text{CV} = \frac{\text{RMSD}}{\text{mean}(\text{obs}^*)} \quad (6)$$

The calculated RMSD and CV, as defined in Equations 5 and 6 include deviations from observations of every trajectory (ensemble member).

For the assessment of DIN profiles of the model, we additionally evaluate RMSD against the monthly mean climatological WOA18 data along the ensembles' mean of trajectories. The monthly WOA18 data are representative for the model trajectories with a 20 km radius. Here, the RMSD are calculated as:

$$\text{RMSD} = \sqrt{\frac{1}{n_m} \frac{1}{n_z} \sum_m^{n_m} \sum_z^{n_z} (\text{mod}_{z,m} - \text{WOA}_{z,m})^2} \quad (7)$$

where $\text{mod}_{z,m}$ and $\text{WOA}_{z,m}$ are monthly averages over trajectories for model results and WOA data, respectively.

2.3.2. Integrated Quadratic Distance

The simulated plankton size spectra are evaluated against those derived from microscopic measurements by applying a non-parametric distance metric. We use the Integrated Quadratic Distance (IQD) (e.g., Thorarinsdottir et al., 2013). In our case it represents a divergence function that describes the difference between the cumulative distribution of normalized biovolumes of all size classes resolved by the model (F_{mod}) and observations (G_{obs}) derived from the normalized, continuous biovolume-size spectra (f_{mod} and g_{obs}):

$$\text{IQD}(F_{\text{mod},v}, G_{\text{obs}}) = \int_s (F_{\text{mod},v}(s) - G_{\text{obs}}(s))^2 ds \quad (8)$$

with s being the log-transformed ESD ($s = \log_{10}(\frac{\text{ESD}}{1\mu\text{m}})$). The IQD is separately calculated for the phytoplankton and zooplankton spectra, distinguishing between the summer and autumn setups as well as between the trajectories origins (Arctic and Atlantic). We note that this metric accounts for relative changes in the community size

structure. Changes in biomass are exclusively assessed as RMSD described before, based on the Chl-*a*, POC, and PON data.

2.4. Model Calibration

Model calibration was performed in two successive parameter estimation steps. In a first step, the sum of residuals between transformed data and model results was minimized, using a genetic algorithm for optimizing parameter values. The transformation was determined by a linear mixed model, based on log-transformed, depth-resolved measurements of different types. We estimated a total of 17 parameters (indicated with “b” in Table 1) in the numerical optimization, of which 12 parameters determine size dependencies in the model. This initial numerical optimization produced unsatisfactory results with respect to cross-comparisons with monthly WOA18 data along the trajectories (data not shown), which were not included in the cost function. Also, the simulated plankton size spectra poorly matched their observational counterparts. Perhaps crucially, as we later realized, the cost function was under-constrained by not imposing non-linear restrictions on combinations of the size-dependent parameters representing minimum nutrient quota, nutrient uptake rate, and photosynthetic rate, as described by Ward et al. (2017).

From a subsequent parameter sensitivity analysis we could identify six model parameters (described below) whose refined values significantly improved the model's ability to reproduce observational data. Therefore, in a second step, we used the parameter estimates from the initial optimisation and adjusted the values of these six parameters, such that the final model solutions show much better agreement with all four different data types, using the RMSD and IQD (Equations 5, 7 and 8) for assessing the model results of: the (a) local tracer concentrations, (b) Chl-*a* remote sensing data, (c) monthly WOA18 climatology, and (d) the plankton size spectra. For these six parameters, we have introduced values that further improve the model solutions in terms of comparability with the observed tracer concentrations. The former values identified in the numerical optimisation are given in square brackets. The minimum nitrogen quota of the autotrophs is set to $Q_{N,a}^{\min} = 0.035$ [0.1423] mol N (mol C)⁻¹, the sinking velocity of detritus is adjusted to be $w_{\text{det}} = 10$ [1] m d⁻¹, and a single remineralization rate of $r_{i,\text{DOM}} = 0.04$ [0.02] d⁻¹ is assigned to the hydrolysis and remineralization of DOC and DON. Furthermore, the size dependency of photosynthesis is modified by refining the exponent of the maximum photosynthetic rate ($P_b^{\max} = -0.08$ [-0.15]). A quadratic mortality is introduced with a value of $m_2 = 0.05$ [0] m³ mmol C⁻¹ d⁻¹ for the largest size class ($j = 9$). Finally, the impact of grazing is refined with a maximum potential prey capture rate G_a^{\max} of 11 [21] d⁻¹.

Manual tuning of model parameters should be unnecessary for any sufficiently constrained model. The parameter values resulting from the numerical optimisation indicated that repeating the first optimisation step while constraining the parameters to ensure that variability in cell growth rate as a function of volume matches observation (based on Ward et al., 2017) may be all that is required to achieve satisfactory model outputs from a purely automated method. Alternatively, there may be need to include the WOA18 data into a single meaningful cost function, alongside the in situ measurements, or to perform a multi-objective optimization with three or even four different metrics for the respective data types. The former of these two options would require additional research efforts while the latter would demand optimization algorithms to be tested according to their usefulness for our special case. Improvement to the numerical optimization routine continues, but goes beyond the scope of this study, so we therefore restrict our analysis to the model solutions identified with the two-step calibration approach.

3. Results

Here, we discuss the model results from different perspectives. We first consider the model solutions along the trajectories and compare them with climatological monthly WOA18 data and with monthly Chl-*a* concentrations derived from satellite measurements. We then focus on comparisons of the local patterns between the HAUSGARTEN data and our model results, distinguishing between variations in vertical tracer distributions and horizontal heterogeneity. The simulated plankton size spectra in the FS are compared with the spectra derived from microscopic measurements. Finally, the temporal developments in the plankton community size structure, of NPP and export are presented as they occur before, during and after the observation periods. In general, all model solutions are obtained with an identical set of parameter values and any differences between these solutions are due to variations in origin and pathway of the individual trajectories. Accordingly, these differences are largest between the four ensembles (summer Arctic, summer Atlantic, autumn Arctic, and autumn Atlantic) and smaller between individual members of an ensemble.

3.1. Data-Model Comparison: Seasonal Patterns of DIN and Chl-*a* Concentrations Along Trajectories

By averaging over all members (trajectories) of an ensemble, we find major differences between the ensembles with respect to the timing and intensity of plankton growth and nutrient utilization. This can be well illustrated by comparing seasonal changes in monthly mean DIN concentration, which can also be assessed against the climatological nitrate concentrations derived from WOA18 data along the trajectories' pathways (Figure 3). When compared with the WOA18 monthly means, the simulated profiles reproduce the vertical distribution and temporal development of DIN concentration in a similar manner. The major discrepancy is a delayed but then more rapid decline in DIN concentration during late spring/early summer in the model solutions. The timing of the DIN decline fits best in Atlantic trajectories of the autumn setup. Furthermore, differences in the vertical structure between our simulations and WOA data are more pronounced below ca. 50 m depth. Especially during the growth season, nitrate concentrations in the model ensembles consistently show a rapid increase with depth, while this increase is considerably more gradual in the respective WOA data. While minimum concentrations in the WOA18 data sporadically fall below 1 mmol m^{-3} in all subsets, similarly low DIN concentrations are only reproduced in model solutions of the autumn setup simulations of the Arctic trajectories.

We furthermore compared simulated Chl-*a* to monthly and 8-day mean concentrations derived from remote sensing along the model trajectories (20 km radius, limited to 2018) in Figure 4. Although similar in magnitude, the timing of the spring bloom along the Arctic trajectories could not be resolved by our simulations. Model solutions of some individual trajectories exhibit a somewhat earlier bloom development, for example, starting by the end of May. The overall delayed bloom development in the simulated Arctic trajectories leads to an overestimation of Chl-*a* concentration in June and July. These discrepancies in Chl-*a* decrease with time, without major deviations occurring in the late summer and early autumn months, when the simulated Chl-*a* concentrations become similar to the remote sensing data. We note that remote sensing estimates for April and May along the Arctic trajectories come with large uncertainties, as ice cover is still extensive during this period, which allows only few observations. These few observations may be biased as they stem from locations with thinner ice cover and therefore more light exposure.

For the Atlantic trajectories, the model solutions are in better agreement with the data. The monthly and 8-day mean Chl-*a* concentrations in June compare well, with similarly good matches in both, the summer and the autumn model setup. This period includes the peak of the bloom in the model results of the summer setup and their counterpart remote sensing estimates. However, in the autumn setup model results in June describe a post bloom stage when the respective remote sensing observations indicate the gradual formation of a bloom that peaks a month later. The best model representation can be assigned to the solutions of the summer setup of the Atlantic trajectories, as they also provide the best fit to the monthly mean WOA18 nitrate concentration data (Figure 3). Daily concentrations of simulated Chl-*a* can exceed the monthly averages by a factor up to two, with some considerable variations between trajectories during the exponential growth phase in June and July (Atlantic summer trajectories), and in May and June in the Atlantic autumn trajectories. We note that the earlier bloom development in the Atlantic autumn ensemble is due to the more southern positions of these trajectories in May, with higher light levels compared to the trajectories of the Atlantic summer setup. The remote sensing Chl-*a* data reveal a small but distinctive bloom in September that is less accentuated in the simulation results. The simulated Chl-*a* concentrations in September are rather a prolongation of the summer conditions. In November the simulated Chl-*a* concentrations of all trajectories, of all four ensembles, drop below 0.05 mg m^{-3} . With the onset of the dark Arctic winter period all photoautotrophic growth becomes inhibited in our simulations.

3.2. Data-Model Comparison: Local Patterns in the Fram Strait

The ensembles of model solutions of the individual trajectories allow us to analyze the range of simulated biogeochemical tracer concentrations within the region of the HAUSGARTEN observatory in the FS during the periods of sampling in 2018.

3.2.1. Local Vertical Distributions

Within the target region, the model reveals greater variability in concentrations of DIN and Chl-*a* than in POC and PON (Figure 5). In particular, the variations in POC and PON observed during the sampling campaigns (summer: 16 July–27 July 2018; autumn: 16 September–4 October 2018) are larger than those explained by the ensembles of model solutions.

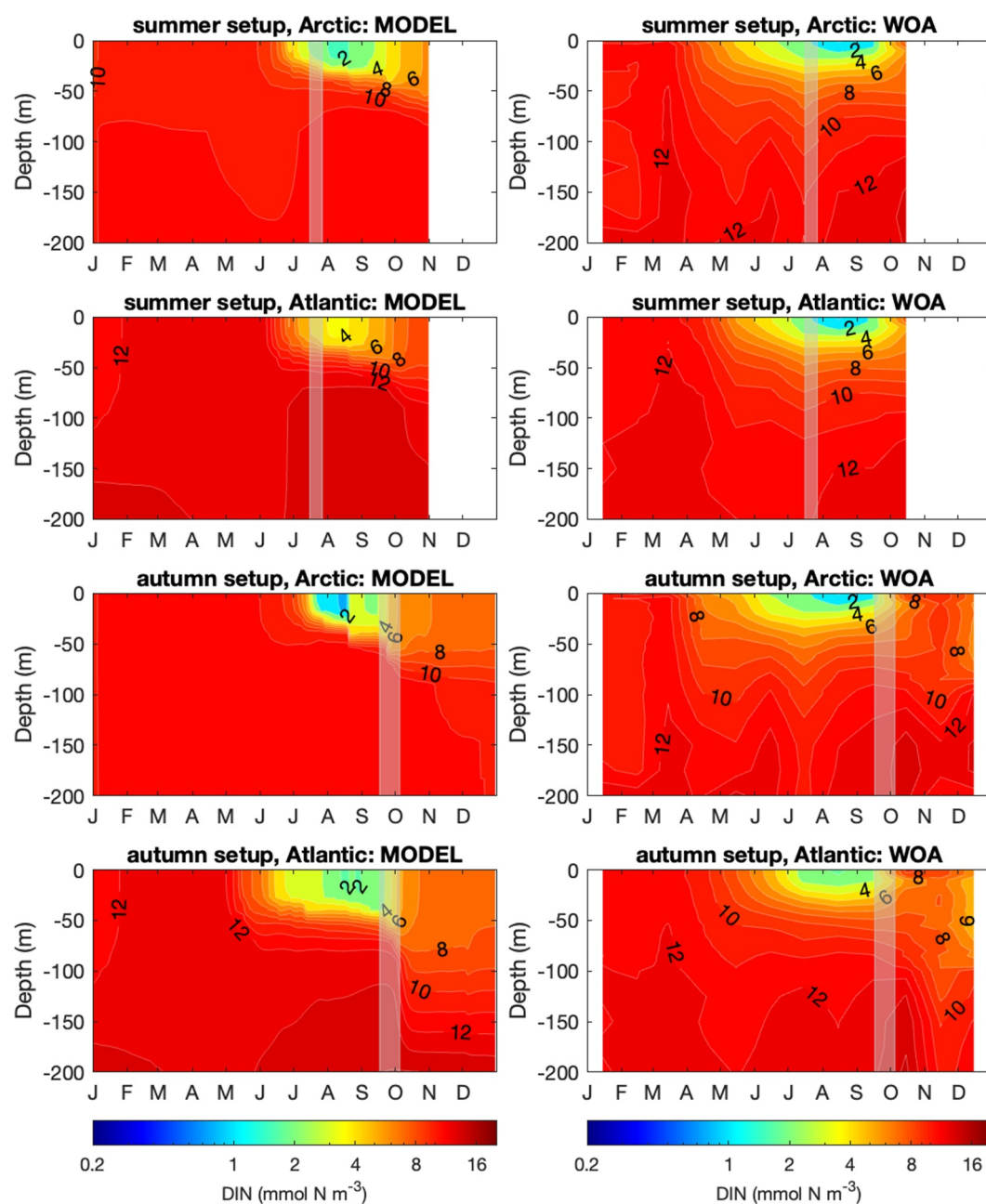


Figure 3. Fit of simulated dissolved inorganic nitrogen to corresponding World Ocean Atlas data. Model results (left column) were averaged over trajectories, discriminating between their Arctic and Atlantic origins. World Ocean Atlas data (right column, Boyer et al., 2018; Garcia et al., 2019) were extracted along the model trajectories for each day with a 20 km radius, then averaged over trajectories.

We calculated the root mean squared deviation and CV (Section 2.3) as a metric for model fit. Averaged values for the seasonal model setups are summarized in Table S1 in Supporting Information S1. The model (in summer setup; no observational nitrogen data for autumn sampling campaign) slightly overestimated DIN concentrations in the upper 100 m. For the in situ comparison, smaller RMSDs and CVs indicate a slightly better fit in the Arctic trajectories than in those coming from the Atlantic. Simulated chlorophyll values in the summer setup in the upper 26 m seem overestimated, however several depth layers with single measurements (the single vertical blue lines in the figure indicate a single observation at the respective depth) are occasionally well above the interquartile range of simulated Chl-*a* concentrations. The fit between 30 and 40 m matches well, and simulated concentrations for

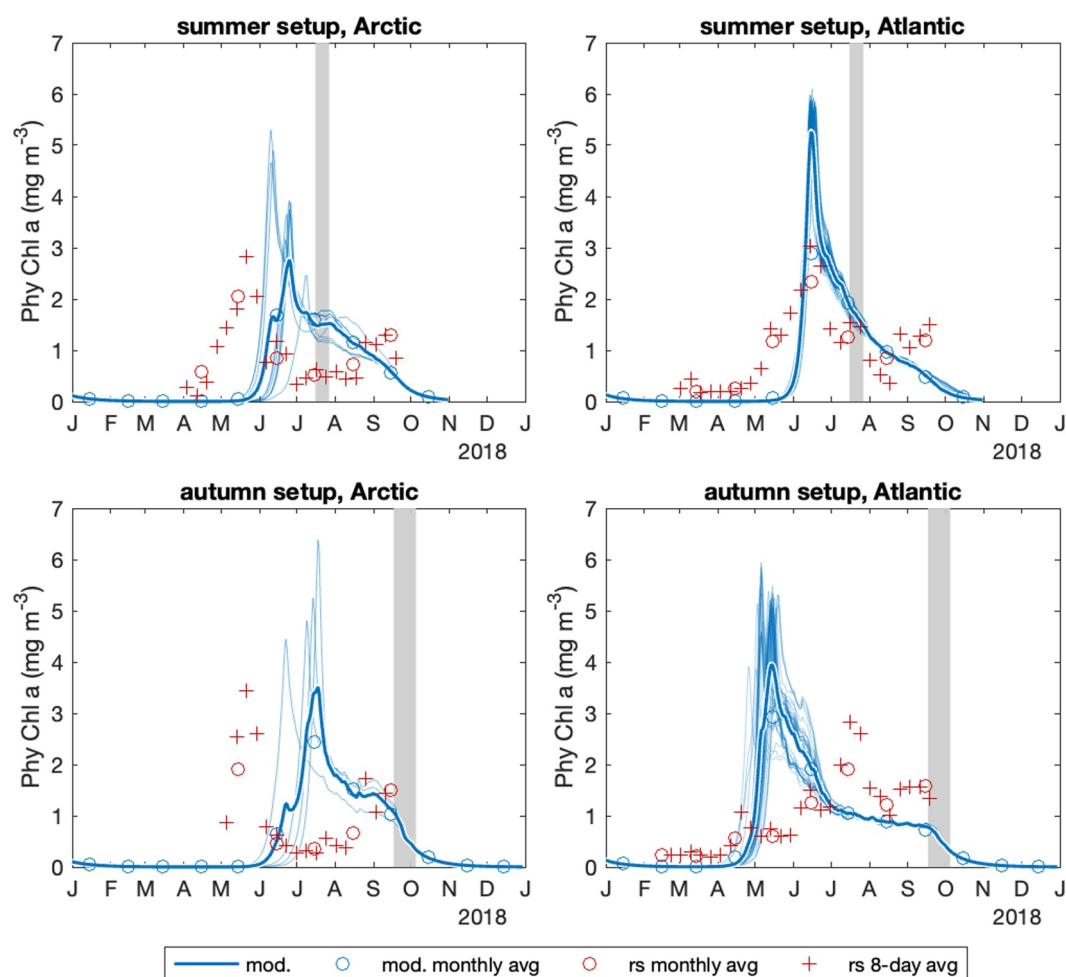


Figure 4. Comparison between simulated Chl-*a* with corresponding remote sensing data. Remote sensing data (monthly means as red circles, 8-day means as red “+” symbols, Sathyendranath et al., 2021) were extracted along the model trajectories with a 20 km radius. The ensemble of thin blue lines represent daily average chlorophyll concentrations over the upper 46 m for individual model trajectories and indicate the variability across trajectories. Bold blue lines represent their respective average over trajectories. Blue circles represent the monthly averages of the (depth and trajectory averaged) simulation results.

depths below 40 m are slightly underestimated. Model-data-fit of Chl-*a* concentrations in the autumn setup is particularly good, although the model produces outliers well above observed concentrations. Both, in summer and autumn, smaller RMSEs and CVs indicate a better fit for Atlantic trajectories. Concentrations of POC in summer and their simulated counterparts fit well, although simulated concentrations below 30 m are rather on the lower end of the observed range. Noticeably, the interquartile ranges of simulated values are smaller than of the observations. The POC data are consistently underestimated during the autumn setup. Simulated PON concentrations were in good agreement with observations in the summer setup (no data for autumn setup).

3.2.2. Horizontal Heterogeneity in Local Tracers

Here we examine the statistical properties of our model solutions and put them into context of the observed horizontal variability (disparities in the measurements between sampling sites in the HAUSGARTEN), using local depth-averaged (upper 100 m) data and model results. The resolved spatial differences are mainly representative for the horizontal heterogeneity, although to some small extent they include short-term temporal variations during the sampling periods, in summer (12 days) and in autumn (19 days). Table 2 documents measures of central tendency as well as 95% confidence intervals (CI95) of concentrations of DIN, Chl-*a*, POC, PON, POC: PON, and DOC_{SL}. The limits of the CI95 represent 2.5% and 97.5% quantiles ($Q_{0.025}$ and $Q_{0.975}$) derived from

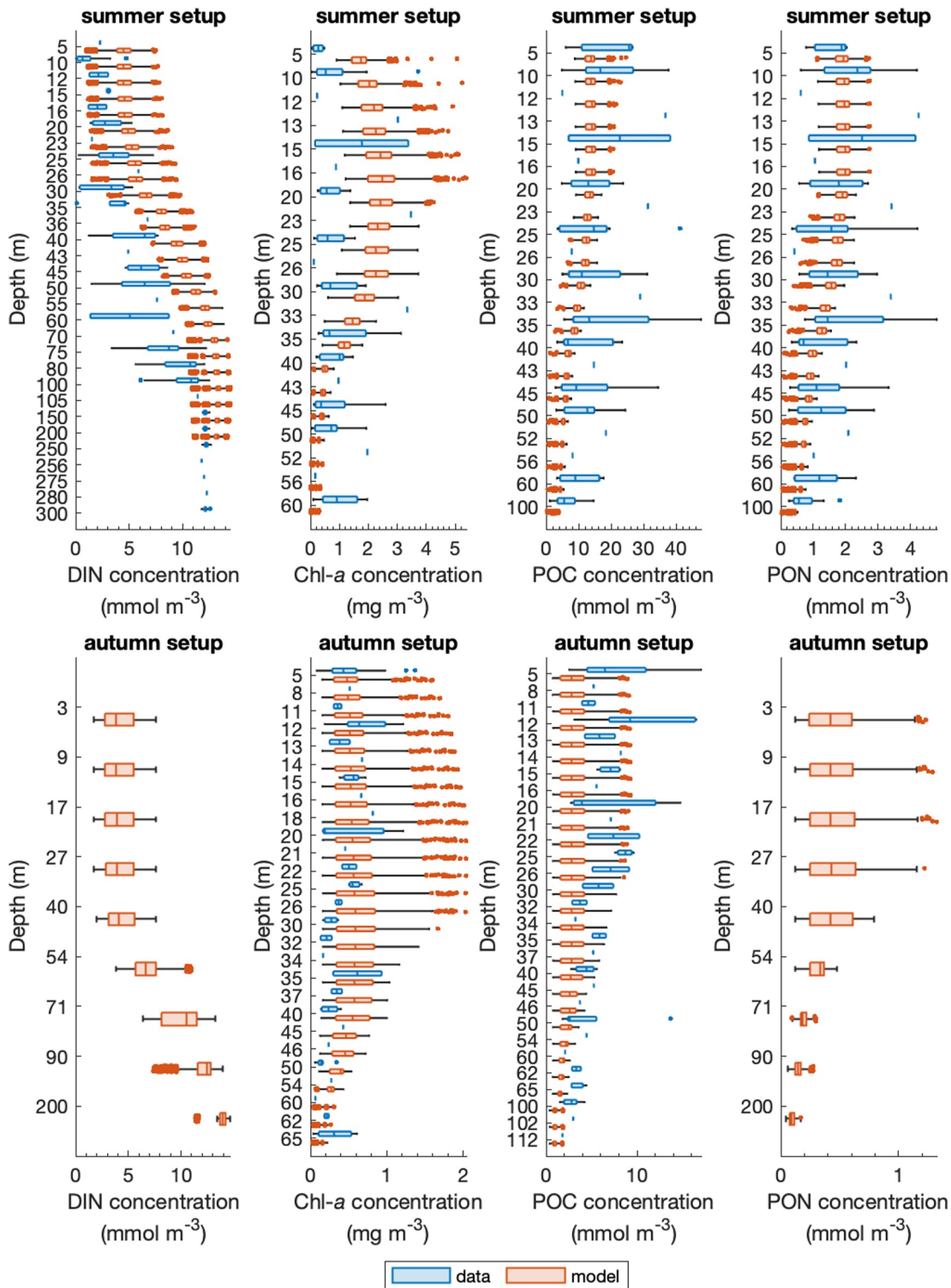


Figure 5. Fit of observed and simulated concentration depth profiles (without water mass distinction; data from Engel et al. (2019) and Torres-Valdés et al. (2019)). Model results (orange) were interpolated to corresponding observation (blue) depths and limited to the time frame when sampling was conducted (summer: 16 July–27 July 2018; autumn: 16 September–4 October 2018) \pm 7 d. No dissolved inorganic nitrogen and particulate organic nitrogen observational data were available for the autumn period. In this boxplot representation, a box represents the interquartile range, the line in the box is the median, and whiskers represent the 99.3% confidence interval (assuming normally distributed data). Single vertical lines with missing boxes are drawn where only individual measurements were available.

Table 2
Measures of Central Tendency and 95% Confidence Limits of Tracer Concentrations, Averaged Over the Upper 100 m, Covering Periods of Observation

Variable/unit, subset	Type	Median	Mean	$Q_{0.025}$	$Q_{0.975}$	$\frac{\Delta CI_{95}^{mod}}{\Delta CI_{95}^{obs}} \times 100$	$\frac{ mean_{obs} - mean_{mod} }{\Delta CI_{95}^{obs}}$
DIN/mmol N m⁻³							
Summer Atlantic	Observed	7.2	7.4	2.4	13.2		
	Simulated	9.8	9.8	8.8	10.6	17	0.22
Summer Arctic	Observed	7.3	7.7	3.6	13.5		
	Simulated	8.2	8.2	7.5	9.4	19	0.05
Autumn Atlantic	Observed	–	–	–	–		
	Simulated	7.2	7.1	6.3	7.8	–	–
Autumn Arctic	Observed	–	–	–	–		
	Simulated	8.0	8.0	7.6	8.3	–	–
Chl-<i>a</i>/mg Chl m⁻³							
Summer Atlantic	Observed	1.4	1.5	0.1	3.3		
	Simulated	0.8	0.8	0.7	1.0	9	0.22
Summer Arctic	Observed	0.4	0.5	0.1	1.0		
	Simulated	0.8	0.7	0.5	0.9	33	0.22
Autumn Atlantic	Observed	0.4	0.4	0.3	0.6		
	Simulated	0.3	0.3	0.2	0.4	50	0.33
Autumn Arctic	Observed	0.4	0.4	0.1	1.0		
	Simulated	0.3	0.3	0.2	0.6	44	0.11
POC/mmol C m⁻³							
Summer Atlantic	Observed	16.2	16.4	5.5	27.8		
	Simulated	7.6	7.5	6.8	8.1	6	0.40
Summer Arctic	Observed	7.1	7.9	1.7	15.0		
	Simulated	6.9	6.7	5.4	7.7	18	0.09
Autumn Atlantic	Observed	4.3	4.5	3.0	6.9		
	Simulated	2.0	2.1	1.2	3.0	46	0.62
Autumn Arctic	Observed	4.0	4.7	2.7	9.3		
	Simulated	2.3	2.3	1.1	3.8	39	0.63
PON/mmol N m⁻³							
Summer Atlantic	Observed	1.8	1.8	0.6	2.9		
	Simulated	1.1	1.1	1.0	1.2	9	0.30
Summer Arctic	Observed	0.7	0.9	0.1	2.2		
	Simulated	0.9	0.8	0.6	1.0	19	0.04
Autumn Atlantic	Observed	–	–	–	–		
	Simulated	0.3	0.3	0.2	0.4	–	–
Autumn Arctic	Observed	–	–	–	–		
	Simulated	0.3	0.3	0.2	0.5	–	–
POC:PON/mol mol⁻¹							
Summer Atlantic	Observed	9.3	9.3	6.9	11.4		
	Simulated	7.0	7.1	7.0	7.3	9	0.49
Summer Arctic	Observed	10.4	10.2	5.0	14.9		
	Simulated	7.8	8.1	7.6	10.5	29	0.21
Autumn Atlantic	Observed	–	–	–	–		

Table 2
Continued

Variable/unit, subset	Type	Median	Mean	$Q_{0.025}$	$Q_{0.975}$	$\frac{\Delta CI95_{mod}}{\Delta CI95_{obs}} \times 100$	$\frac{ \text{mean}_{obs} - \text{mean}_{mod} }{\Delta CI95_{obs}}$	
Autumn Arctic	Simulated	6.6	6.6	6.4	6.8	–	–	
	Observed	–	–	–	–	–	–	
DOC_{SL}/mmol C m⁻³	Simulated	6.7	6.7	6.5	7.0	–	–	
	Summer Atlantic/Arctic	Observed^a	–	6.2	2.8	9.7	–	–
	Atlantic	Simulated	5.5	5.5	5.1	5.9	12	0.10
	Arctic	Simulated	5.9	5.7	4.2	7.0	41	0.07
	Autumn Atlantic/Arctic	Observed^a	–	2.5	1.9	3.1	–	–
	Atlantic	Simulated	1.9	1.9	1.4	2.3	76	0.50
	Arctic	Simulated	3.0	3.1	1.7	4.7	254	0.50

Note. Median and the limits of the 95% confidence interval (CI95) were calculated as quantiles (Q) from cumulative probability densities derived from Kernel density estimates: Median = $Q_{0.5}$, lower ($Q_{0.025}$) and upper ($Q_{0.975}$) limits of the CI95, and $\Delta CI95 = Q_{0.975} - Q_{0.025}$. $\frac{\Delta CI95_{mod}}{\Delta CI95_{obs}} \times 100$ relates the variability found in the model to the observed variability (in%). $\frac{|\text{mean}_{obs} - \text{mean}_{mod}|}{\Delta CI95_{obs}}$ relates the difference of the observed and simulated means to the observed variability. Values printed in bold font refer to observations, those in regular font to simulations. ^aFor the 95% confidence limits we use the z-score together with the standard deviations published in von Jackowski et al. (2020b).

cumulative Kernel density estimates of the respective data, estimated using a diffusion based diffKDE (Pelz et al., 2023). Accordingly, the width of the interval is $\Delta CI95 = Q_{0.975} - Q_{0.025}$.

In general, the medians and means of the model results fall into the CI95 of the observations. Comparisons between the simulated and observed mean concentrations reveal biases that correspond with the differences already seen in the vertical profiles (Figure 5); the model's tendency to underestimate measured PON and POC concentrations while the means of the simulated DIN concentrations (between 8.2 and 9.8 mmol N m⁻³) are higher than the observational means (between 7.4 and 7.7 mmol N m⁻³). The simulated means of the POC:PON ratio are generally lower than observed, between 7.1 and 8.1 in the model results and 9.3 and 10.2 in the observations. With regard to the DOC_{SL} accumulation in summer and the subsequent drawdown until autumn, the model results compare well with the observed concentrations. In all cases, the biases (i.e., the differences between means of observations and simulations) are smaller than the observed variability, as documented in $\frac{|\text{mean}_{obs} - \text{mean}_{mod}|}{\Delta CI95_{obs}}$ in Table 2.

When comparing the CI95, and as indicated by the upper CI95 limits ($Q_{0.975}$), a noticeable finding is that only in the solutions of the autumn-Arctic trajectories the simulated maxima in DOC_{SL} concentration ($Q_{0.975} = 4.7$ mmol C m⁻³) exceed the observed range ($Q_{0.975} = 3.1$ mmol C m⁻³). In all other cases, the $Q_{0.975}$ limits of the observations are higher than in the model solutions, which is even true in the case of DIN, although the model overestimates the observational means. Ultimately, the concentration range of simulated DIN, Chl-*a*, POC, and PON, as well as the variations in POC:PON ratio, do not cover the full range ($\Delta CI95 = Q_{0.975} - Q_{0.025}$) derived from the depth-averaged observational data. Thus, the model's ensemble solutions of the trajectories can explain only a portion of the observed horizontal variability of the HAUSGARTEN data.

To put the variability of the model solutions in relation to the variations found in the observations, we set the widths of the respective CI95 in relation to each other ($\Delta CI95_{mod}/\Delta CI95_{obs} \times \sim 100$), see Table 2. For the summer period, the model trajectories approaching the FS from the north (Arctic) describe a greater portion of the observed horizontal variability (18%–41%) than those of the Atlantic entering from the south (6%–17%). The relative portions are generally larger in autumn (39%–76%), in addition to the higher than observed $Q_{0.975}$ in the simulated DOC_{SL} concentration of the Arctic trajectories (254%) mentioned before. There are two reasons why a larger portion of the horizontal variability within the target region can be explained by the model trajectories arriving in autumn. On the one hand, the observed and simulated OM concentrations are generally lower in autumn than in summer and the widths of the CI95 become narrower. On the other hand, the model trajectories that arrive in autumn are associated with longer pathways, and thus more divergent histories of plankton growth, than the summer trajectories. This is consistent with the finding that the CI95 of the autumn data of Chl-*a* and

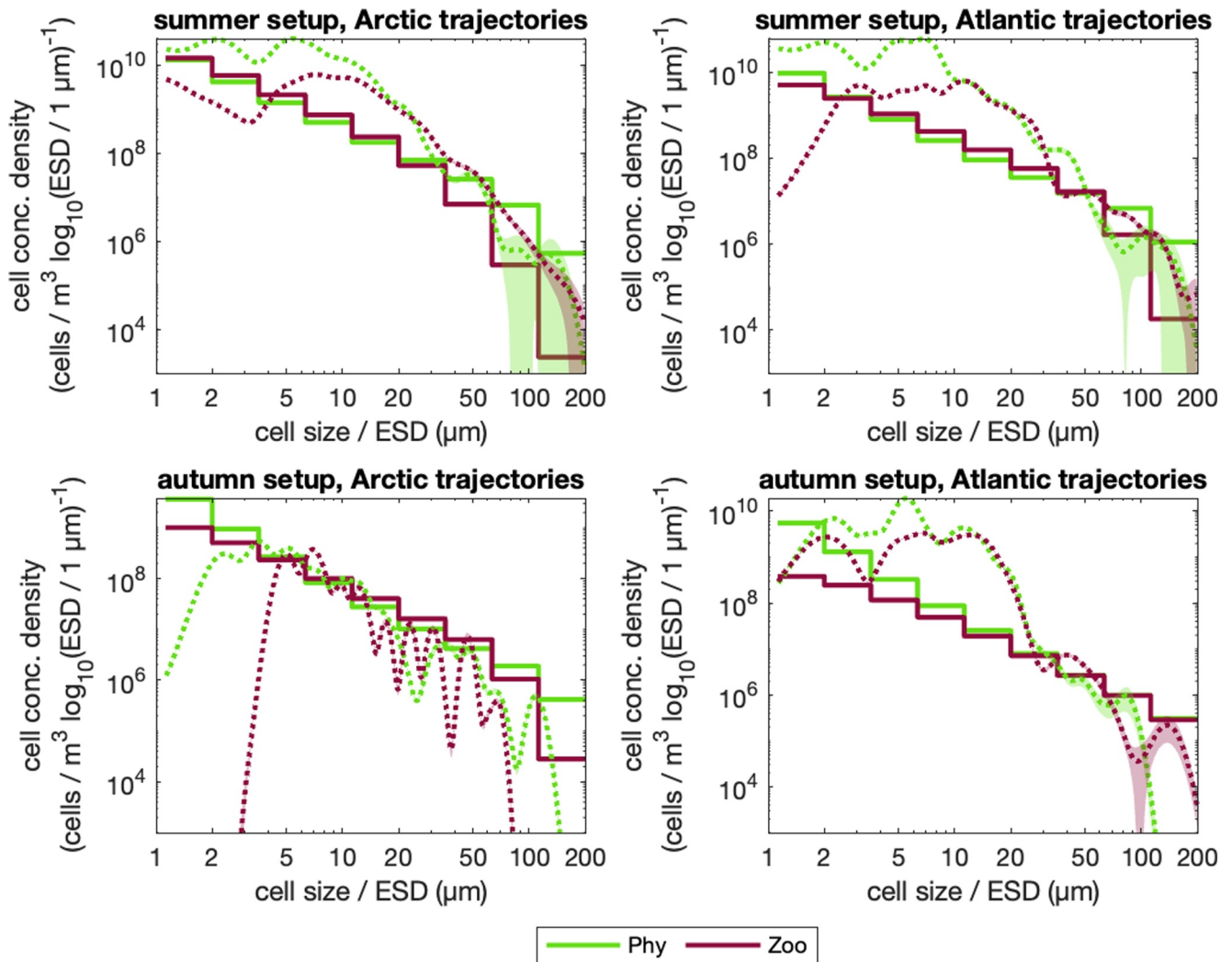


Figure 6. Comparison of simulated plankton size spectra (during sampling period) and observations (Lampe et al., 2021). Model results were extracted for the sampling period ± 7 d and averaged over the upper 46 m. Cell concentrations were derived from C-biomass per size class divided by the respective carbon quota (cell conc. $[\text{cells m}^{-3}] = B_{C,j} [\text{mmol C m}^{-3}] / Q_C [\text{mmol C cell}^{-1}]$). Lines show the mean cell concentration densities (over model trajectories or in situ samples) of phyto- and zooplankton, respectively, with shaded areas indicating the 95% confidence intervals (mean $\pm 1.96 \cdot$ standard error). The confidence limits of the model are narrower than the width of the lines. The dotted graphs represent the observations, the solid lines represent the simulated (size binned) spectra.

POC in the WSC and the corresponding model results (Atlantic trajectories) are narrower than those associated with the EGC (Arctic trajectories). The autumn Atlantic trajectories expand over greater distances, covering a larger latitudinal range.

When comparing the horizontal heterogeneity observed with the spread of depth-averaged solutions obtained with the ensembles of trajectories, some additional insight can be gained by simple comparisons of the non-parametric probability densities (PD) obtained by Kernel density estimation, see Figure S5 in Supporting Information S1. These PDs illustrate the results presented above, particularly with regard to the different widths of the CI95. However, they also show details such as bimodalities and the skewness in the PDs.

3.2.3. Local Plankton Community Size Structure

To evaluate how well the model resolves the size composition of the plankton community, we compare simulated plankton size spectra to continuous size spectra derived from microscopic counts and size measurements (expressed as ESD), as described in Lampe et al. (2021), based on samples collected during summer and autumn. Figure 6 shows that the overall slopes of simulated size-abundance spectra around the time of in situ sampling are

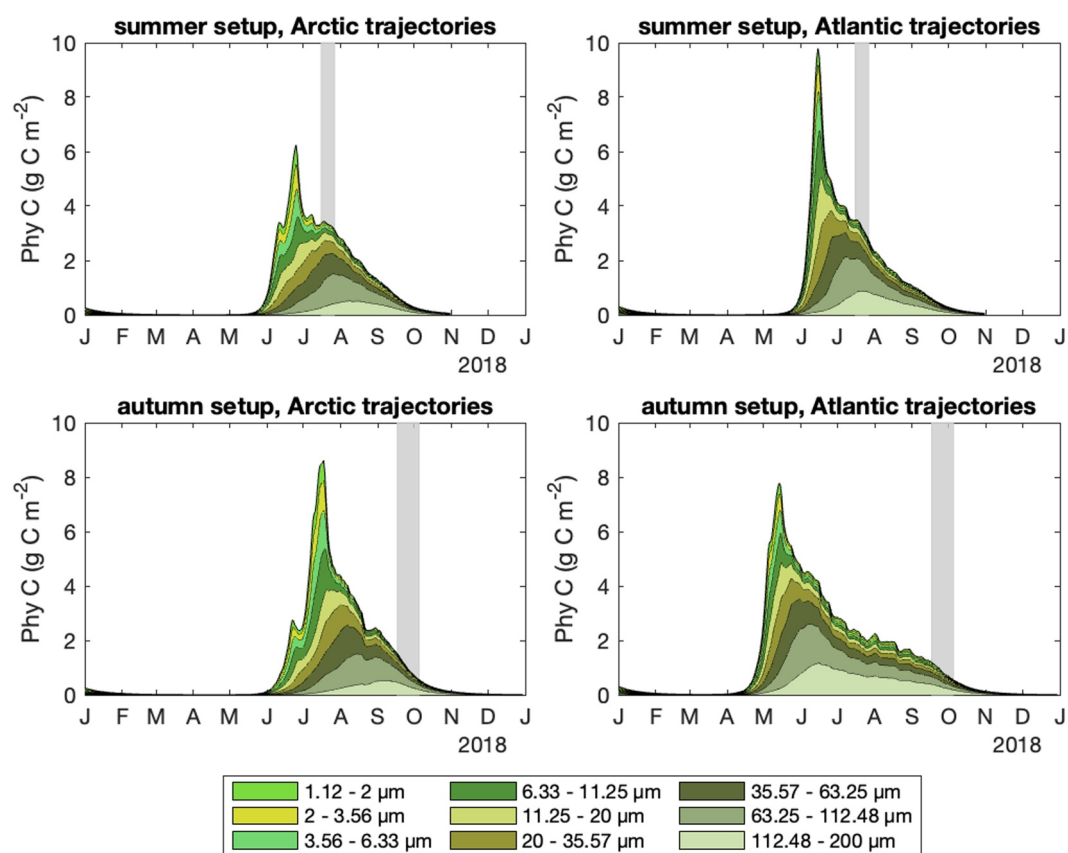


Figure 7. Integrated phytoplankton biomass per size class over time. C-biomass was integrated to 100 m depth and averaged by trajectory origin. Phytoplankton size classes are represented by green colors, and their respective sum equals total phytoplankton biomass.

in agreement with observations. Spectra of total biovolume by size are shown in Figure S1 in Supporting Information S1. Despite this satisfactory general characteristic, the observations in the size range between 4 and 40 μm clearly differ from the simulated almost log-linear relationship (with a nearly constant slope). The solutions of the autumn setup of the Arctic trajectories are the only exception, which instead show a higher abundance of cells with ESD below 2 μm in the simulations. This is all the more interesting because it is this setup in which the total abundance of phytoplankton (sum of all size classes) agrees well with the observations. In all other cases, total abundance is generally underestimated by our model solutions at times of the sampling period. Within the mentioned size range between 4 and 40 μm , the deviations can be as high as a factor of 10 in the trajectories of the summer setup, and even higher (almost factor 20) in the autumn setup of the Arctic trajectories. We note that the deviations in the size spectra are not accompanied by serious discrepancies compared to the PON and POC data shown before; data that were used as constraints for the total biomass.

3.3. Temporal Variations in Community Size Structure of the Plankton

The relative size distributions and the corresponding total phytoplankton biomass of our model solutions resolve distinctive seasonal patterns (Figure 7). The simulated blooms in the Arctic trajectories reveal two distinct peaks associated with the spring bloom. Some minor first peaks occur in early June (summer setup with 3 g C m^{-2}) and mid-June, with approximately 2.5 g C m^{-2} in the autumn setup. These first peaks are followed by stronger peaks, only three and 4 weeks later in the summer and autumn setups of the Arctic trajectories respectively. Both maxima differ in their magnitude. Those trajectories that approach the FS in autumn yield maxima of around 8.5 g C m^{-2} . In the summer setup, the total phytoplankton biomass reaches 6 g C m^{-2} during the bloom. According to our model results, the blooms along the EGC are later but more intense the further north they are, away from the HAUSGARTEN region. Apart from the double peaks, we obtain a characteristic that is consistent with this result

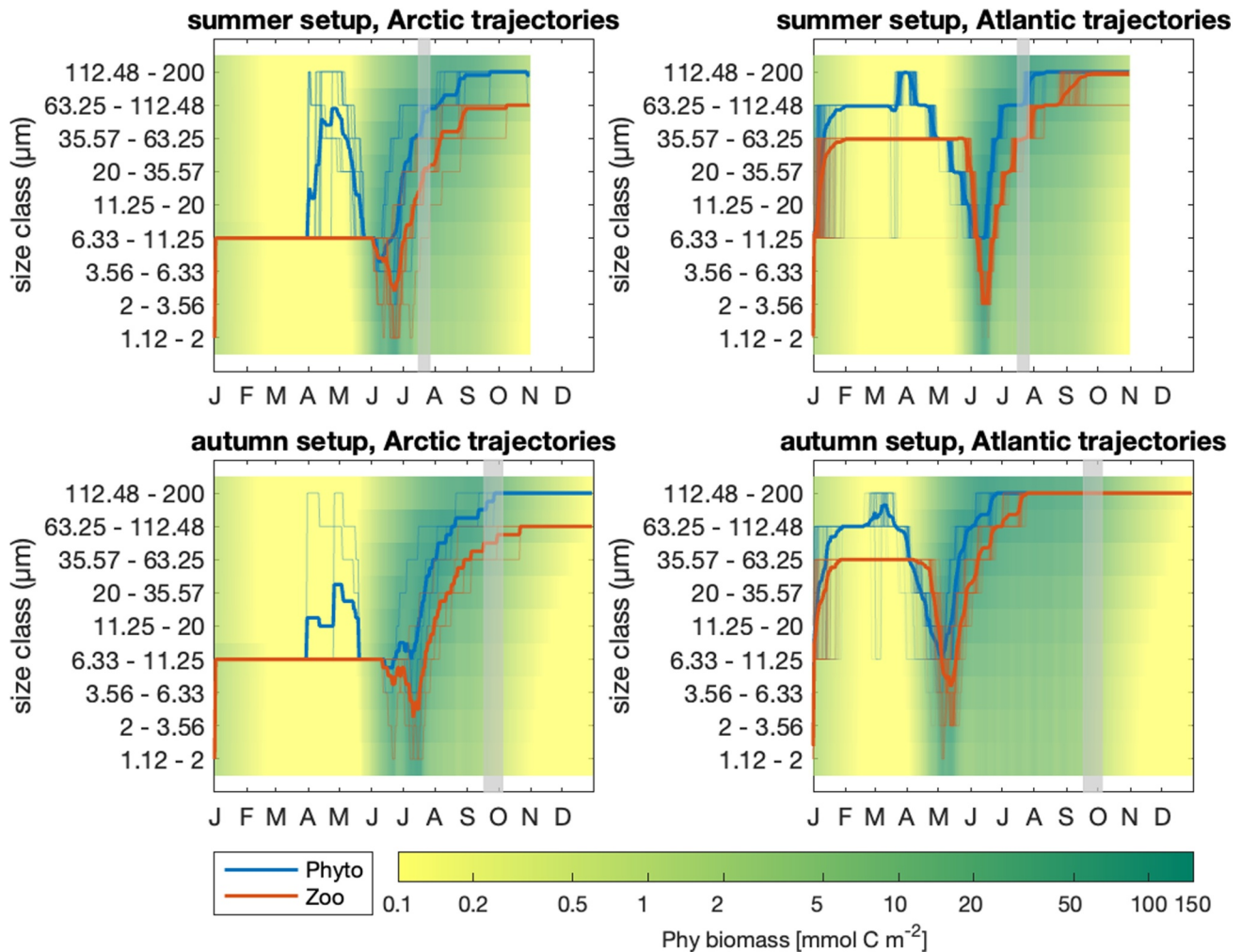


Figure 8. Size classes with maximum biomass for phytoplankton (blue) and zooplankton (orange) over time, integrated over the upper 46 m. Translucent lines represent single trajectories, solid lines the trajectory-mean (calculated from the respective size class indices). Background colors indicate the depth-integrated phytoplankton biomass per size class.

for the Atlantic trajectories coming from the south. The difference is that the Atlantic trajectories starting further south show the earlier bloom, which is the case for the autumn setup with a maximum of almost 8 g C m^{-2} .

Here, too, the later bloom in the Atlantic trajectories of the summer setup is accompanied by a higher intensity, reaching almost 10 g C m^{-2} in mid-June. These trajectories approach the FS in summer and therefore originate further north than the trajectories that do not arrive there until autumn. Thus, the summer Atlantic trajectories are always north of the corresponding autumn trajectories and they are thus exposed to lower light levels during the spring period. Overall, all the results together suggest that it is predominantly the availability of light within the mixed layer that determines the temporal bloom development in these high latitudes in these simulations. We note that short-term (e.g., diurnal) stratification events remain unresolved in this model; a process that could counteract light-limitation of phytoplankton growth. Considering the predominant role of light exposure in the presence of short-term stratification (e.g., within ice and snow covered regions), this could explain why the simulated blooms are delayed in the Arctic trajectories, as previously described (Figure 4).

The shift of plankton biomass towards larger size can be well demonstrated by depicting the temporal variations of the most dominant class (Figure 8). The figure shows the size class that comprises the maximum carbon concentration of all nine size classes, of the phytoplankton and the zooplankton respectively. In general, temporal changes in dominant size class show greater similarities between trajectories that share the same origin than between the different seasonal model setups. During the initial growth phase, when light is the only limiting factor

Table 3
Time and Depth-Integrated (100 m) Net Primary Production, Export of Carbon (C) and Nitrogen (N) at 100 m, and Export Efficiency (Pe-Ratio)

Data subset (ensemble)	Production [$\text{g m}^{-2} \text{yr}^{-1}$]		Export [$\text{g m}^{-2} \text{yr}^{-1}$]		Pe-ratio	
	C	N	C	N	C	N
Summer/Arctic	53.14 ± 6.34	7.11 ± 0.87	22.16 ± 3.17	3.23 ± 0.46	0.42 ± 0.01	0.45 ± 0.01
Summer/Atlantic	61.04 ± 0.93	9.01 ± 0.19	28.02 ± 0.65	4.40 ± 0.14	0.46 ± 0.01	0.49 ± 0.01
Autumn/Arctic	69.04 ± 1.39	8.69 ± 0.44	27.37 ± 2.38	3.79 ± 0.38	0.40 ± 0.03	0.44 ± 0.02
Autumn/Atlantic	100.96 ± 5.67	15.04 ± 0.77	50.15 ± 2.73	7.85 ± 0.43	0.50 ± 0.01	0.52 ± 0.01

Note. Values are the model ensemble means ± standard deviation.

and while total biomass remains low (below $0.2 \text{ mmol C m}^{-2}$), all solutions have in common that they initially favor the growth of larger phytoplankton cells. The larger cells are more efficient than the smaller sized phytoplankton during this early low light pre-bloom period, because of their high nutrient uptake rate (v^{max}) relative to carbon fixation. This advantage is only of short duration and the considerable build-up of biomass at the onset of the bloom is then actually achieved by phytoplankton of all size classes, with smaller-to-intermediate size classes ($3.6\text{--}6.3$, $6.3\text{--}11.3 \mu\text{m}$) accounting for the largest proportion. During the summer months, the highest growth rates occur in these small-to-intermediate size classes, but the gradual shift towards a dominance of larger phytoplankton is mainly controlled by top-down processes.

In the Arctic and the Atlantic trajectories, the zooplankton respond to the food availability in the smaller size range. Clearly, the temporal fluctuations in the predominant size class of zooplankton are a delayed response signal that follows the predominant size class of phytoplankton after about one to 3 weeks. Once zooplankton stocks sufficiently increased, the grazing progressively depletes populations of small phytoplankton. Following the peak in total biomass, more and more biomass shifted to larger size classes as total biomass declined. Most biomass end in the largest size class ($112\text{--}200 \mu\text{m}$), at times when total biomass has decreased below $2\text{--}3 \text{ mg C m}^2$. Apart from the Arctic autumn trajectories, most zooplankton biomass is found in the largest size class, roughly one month after phytoplankton have reached their maximum size class in the Atlantic trajectories. In the Arctic trajectories, the largest dominant sizes of the zooplankton range within the eighth size class ($63\text{--}112 \mu\text{m}$). This size class becomes dominant in September in the summer setup and in October in the autumn setup.

3.4. Temporal Variations in Net Primary Production and Export of Carbon and Nitrogen

Our analyses of the annual, depth-integrated NPP, the POM export at 100 m, and the corresponding export efficiency along the model trajectories reveal clear differences between the ensembles (Table 3). The temporal variations are more pronounced in NPP than in export, also revealing greater variability in the Arctic than in the Atlantic trajectories (Figure 9).

With $101 \text{ g C m}^{-2} \text{yr}^{-1}$ we find the highest productivity in the Atlantic trajectories of the summer setup, where light availability is highest. Compared to the Arctic trajectories, the NPP in the trajectories of Atlantic origin is generally higher (Table 3). Despite the overall lower NPP, the spatio-temporal variability in NPP is higher along the Arctic trajectories, in particular at times when the bloom begins, which is due to extensive fluctuations in temperature rather than in surface irradiance (see Figure 2). Generally, our model results yield lower C:N ratios in yearly production rates in the Atlantic ensembles (summer: 7.9; autumn: 7.8) than in the Arctic ensembles (summer: 8.7; autumn: 9.3). Surprisingly, and despite the previously mentioned differences, the ensemble mean values of NPP appear to have converged during the observation periods and show similar values between the Atlantic and Arctic trajectories: Arctic (NPP = 54 ± 11 and $5 \pm 4 \text{ mmol C m}^{-2} \text{d}^{-1}$, summer and autumn respectively), Atlantic (NPP = 56 ± 8 and $6 \pm 4 \text{ mmol C m}^{-2} \text{d}^{-1}$).

Generally, export is closely related to NPP and follows it with a lag of 2–3 weeks. The rapid increase in productivity in spring is not immediately reflected in exports, suggesting that much of the spring production remains in the upper ocean and is recycled rather than being rapidly exported to depth. The high temporal variability in the export in Arctic trajectories is linked to the high variability in NPP. Furthermore, the spatial variability in NPP, that is strongly expressed in Atlantic trajectories of the summer setup, propagates to export. During September,

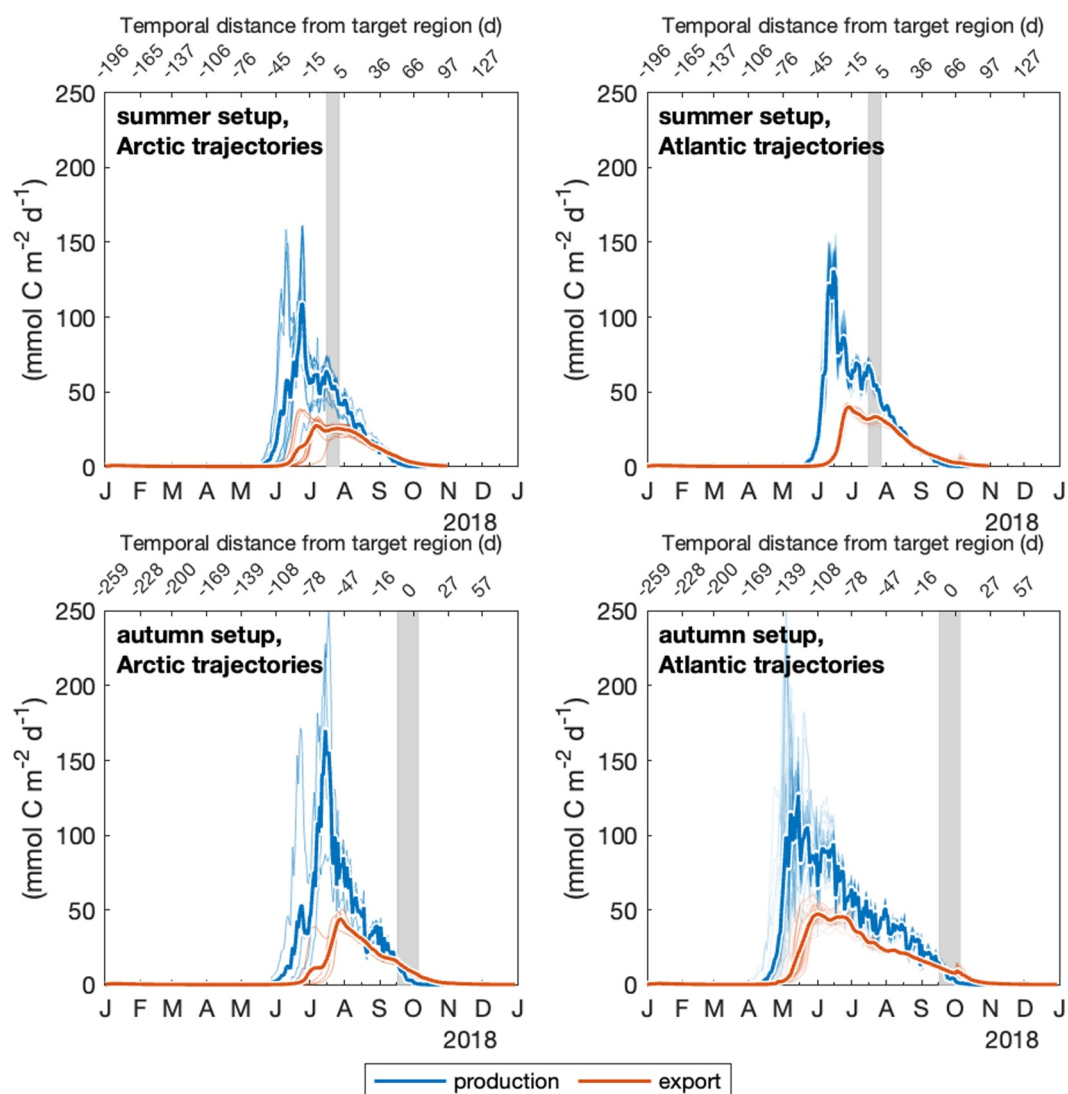


Figure 9. Depth-integrated carbon production (blue) and export (orange) at depth (100 m). Bold graphs indicate the mean between all Arctic (left panels) and Atlantic (right) model trajectories. Thin lines show the values of individual trajectories. Upper panels show the results from the summer model setup, lower panels from autumn setup. The timespan of the passage of HAUSGARTEN and of in situ sampling is highlighted in gray.

export begins to exceed local production. The productivity is always higher in the Atlantic than in the Arctic trajectories, which translates into higher annual export accordingly, with a maximum of $50 \text{ g C m}^{-2} \text{ yr}^{-1}$ in the Atlantic summer setup. As for the NPP, the C:N ratios of the yearly export rates are lower for the Atlantic ensembles (7.4 for both, summer and autumn setups) than in the Arctic counterparts (summer: 7.9; autumn: 8.4). Although not as striking as in case of NPP, during the sampling periods, the export flux at 100 m do not differ much in Arctic (Export = 24.8 ± 3.6 and $10.4 \pm 2.8 \text{ mmol C m}^{-2} \text{ d}^{-1}$ in summer and autumn respectively) and Atlantic (Export = 32.5 ± 1.5 and $9.1 \pm 1.8 \text{ mmol C m}^{-2} \text{ d}^{-1}$) trajectories. These differences are small despite the preceding developments in export flux exhibit larger differences (Figure 9).

The efficiency of export integrated over the productive period is slightly higher in the solutions of the Atlantic ensembles, indicating less efficient export and thus more retention and recycling takes place in Arctic trajectories. Differences in the pe-ratio of C and N are, albeit small, caused by the variable stoichiometry in the model. The model solutions indicate some marginally more efficient export of N than of C. We note that the rates assigned to demineralization in our model are identical for C and N, which means that the difference here only reflects the higher C:N ratio of the OM that is demineralized. Instant, daily pe-ratios show a considerable temporal and spatial

variability (Figure S4 in Supporting Information S1). While in the beginning of the productive period pe-ratios are close to 0, they increase to 0.4–0.6 in Arctic trajectories and 0.4–0.8 in Atlantic trajectories during the summer sampling period and eventually exceed 1 during the autumn sampling period. An instant pe-ratio greater than one is due to the continuation of export, here at 100 m, of POM that has already been produced before, while at the same time the actual productivity gradually ceases.

4. Discussion

As water parcels move through space over time, they are subject to varying environmental conditions, such as light availability, temperature, and water column stratification. Studies in the HAUSGARTEN observatory that present time series of biogeochemical measurements (e.g., Engel et al., 2019; Nöthig et al., 2015, 2020) reveal substantial variability in the data, with differences between samples at individual times and locations. Some part of the variability seen in the local observations can be attributed to water masses that are passing by the sampling stations and are thus “snapshots” of the current situation. To relate observed changes, for example, in plankton composition, to changes in local physical and biogeochemical conditions is difficult, since the specific conditions to which the communities were exposed before their arrival in the observation region remain unresolved. The Lagrangian modeling approach allowed us to investigate bottom-up and top-down processes that determine seasonal changes along trajectories. With our simulations of distinct ensembles of trajectories we could analyze a large suite of model solutions (with different histories in space and time) and examine how these can contribute to the variability seen in the pelagic ecosystem at HAUSGARTEN in the FS at times of observation. Furthermore, we determined the spatio-temporal variations along the major trajectories passing the FS.

This section discusses the representativeness and usefulness of our model solutions. We address the insights gained on the different distributions (spatial and temporal) of the trajectories, focusing on NPP and POC export. We further elucidate aspects of the compositional variations of the plankton. The differences in DOM and POM, as resolved by our simulations, are discussed in relation to the concentrations typically observed in the FS. Finally, we explain the limitations of the model as well as potential improvements.

4.1. Influence of Trajectory Origin and Evolution on NPP and POC at HAUSGARTEN Sites

Trajectories emanating from the North Atlantic cover a wide latitudinal range of 15° or up to 1,930 km in summer and as much as 17° (2,100 km) in autumn. The Arctic trajectories cover only a range between 5.5° (650 km) and 6.7° (830 km) latitude (autumn and summer setup respectively, see Figure 1. In Section 3.2.2 we show that a significant part (6%–17% in Atlantic and 18%–41% in Arctic trajectories of the summer setup; 46%–76% in Atlantic and 39–44 (254)% in Arctic trajectories of the autumn setup) of the variability in tracer concentrations observed locally at HAUSGARTEN is caused by differences in the pathways of water parcels passing the HAUSGARTEN sampling sites. Here we discuss how our estimated rates of NPP and export in the FS compare with those derived from observations and other modeling studies, and document how these rates change along the trajectories resolved in our model.

Our model results of annual NPP are within the range of rates reported for the FS from observations and modeling studies. The ensemble means of NPP in the FS of the Atlantic trajectories are 61.0 ± 0.9 (summer setup) and 101.0 ± 5.7 (autumn setup) $\text{g C m}^{-2} \text{ yr}^{-1}$ (Table 3). The corresponding Arctic trajectories (along the EGC) yield mean rates that are slightly lower, 53.1 ± 6.3 (summer setup) and 69.0 ± 1.4 (autumn setup) $\text{g C m}^{-2} \text{ yr}^{-1}$. Arrigo and Van Dijken (2011) derived an average NPP for the Greenland Sea of 86.0 ± 6.5 $\text{g C m}^{-2} \text{ yr}^{-1}$ from long-term remote sensing analysis between 1998 and 2009, while Hop et al. (2006) reported an average rate of 80 $\text{g C m}^{-2} \text{ yr}^{-1}$ for the FS. Similar to our results, Wassmann et al. (2010) found GPP to be higher in the eastern than in the western part of the FS in their SINMOD simulations (east: $\text{GPP} \approx 130$ $\text{g C m}^{-2} \text{ yr}^{-1}$, and west: 50 $\text{g C m}^{-2} \text{ yr}^{-1}$). Net primary production estimates obtained in SINMOD simulations were considerably lower, as documented in Vernet et al. (2021), and yield an NPP of 33.2 $\text{g C m}^{-2} \text{ yr}^{-1}$ in the EGC dominated region of the FS. For the same region, even lower rates of NPP (11 $\text{g C m}^{-2} \text{ yr}^{-1}$) were derived from their remote sensing data analysis, which is roughly equivalent to only 18% of NPP in our results. However, we like to note that the study of Vernet et al. (2021) focused on coastal waters off Greenland and the high ice cover in this region may contribute to the lower NPP estimates compared to our area of interest.

Peaks in productivity occur well before the trajectories reach HAUSGARTEN, as shown in Section 3.4. The time difference is shorter for the summer setup (20–40 days for Arctic; 30–40 days for Atlantic trajectories) than the

autumn setup (ca. 70 days for Arctic and 130–140 days for Atlantic trajectories). During these productivity peaks, our model estimates the maximum daily NPP (integrated to 100 m) around 150–250 mmol C m⁻² d⁻¹, which is within the range reported by Forest et al. (2010) (maximum GPP: 1.5–2.3 g C m⁻² d⁻¹, thus ca. 125–190 mmol C m⁻² d⁻¹), but considerably higher than estimations around 0.6 g C m⁻² d⁻¹ (thus 50 mmol C m⁻² d⁻¹) for the EGC-influenced sector (Vernet et al., 2021). While the timing of the productivity increase is relatively homogeneous within Atlantic trajectories, it is much more variable for Arctic trajectories. Although the average of Arctic trajectories has a slightly later maximum than in the Atlantic trajectories, productivity peaks already in early June in few Arctic trajectories (Figure 9). Arctic trajectories are subject to variations in sea ice cover, while Atlantic trajectories remain ice free throughout the simulated period. Sea ice strongly influences the light available in the water column, which is reflected in the high variability in the start date of the spring bloom in Arctic trajectories in the summer setup. Similarly, Banas, Zhang et al. (2016) found that in the East Bering Strait, bloom timing was controlled mainly by light availability and the light availability was in turn controlled by ice cover in regions under high ice influence, whereas in the ice-free regions, a composite of surface light availability and diffusivity correlated to the bloom timing. Long-term remote sensing observations of Chl-*a* concentrations between 1998 and 2012 typically show maxima around May or June in the EGC and around June or July in the WSC influenced region of the FS (Nöthig et al., 2015). Furthermore, Vernet et al. (2021) report the initiation of the bloom between late May and mid-June for the North-East region off Greenland, which is similar to our simulations.

The temporal delay in NPP and export signals leads to the accumulation of POC at different times and distances from the target region, as shown in Figure 10. In the ensembles of trajectories passing HAUSGARTEN during the summer sampling period, POC concentrations reach their highest levels just before entering the HAUSGARTEN region (in situ sampling stations are marked with black “+” signs). During this time, within the 77.5°N–80°N latitude bin, NPP (31.7 mmol C m⁻² d⁻¹ in Arctic and 28.2 mmol C m⁻² d⁻¹ in Atlantic trajectories) and export (11.4 and 13.6 mmol C m⁻² d⁻¹) average fluxes are highest. Export exceeds NPP once the Atlantic trajectories leave the target region. In contrast, in the autumn setup, where trajectories cross HAUSGARTEN during the autumn sampling period, the maxima in POC concentration, NPP, and export occur before the Atlantic trajectories enter the target region. In the Atlantic-autumn ensemble, we observe the highest POC concentrations about 5° south of HAUSGARTEN, and the concentrations have decreased considerably by the time the trajectories reach the region. Similarly, in the Arctic-autumn ensemble, NPP and POC reach their highest values before the trajectories approach the HAUSGARTEN region, but the distance is shorter than in the Atlantic counterparts and export is highest in the 77.5°N–80°N latitude bin.

Although our estimations of NPP and tracers (see Sections 3.2 and 4.3) are within the range of observations, our model considerably overestimates export. The annual average of POC export fluxes at HAUSGARTEN between 2000 and 2013, as observed with sediment traps in 200 m depth, ranged from 0.16 to 0.18 mol C m⁻² yr⁻¹ (Salter et al., 2023), which is equivalent to 1.92–2.16 g C m⁻² yr⁻¹. Bauerfeind et al. (2009) reported similar values, with POC fluxes between 1.6 and 2.5 g C m⁻² yr⁻¹ measured with sediment traps in 200–300 m depth. However, our model estimations at the 100 m depth horizon are 10–20 times higher than these observations. Our estimations for POC export at 300 m depth are about half of those simulated at 100 m (Summer Arctic: 12, Atlantic: 16; Autumn Arctic: 15, Atlantic: 28 g C m⁻² yr⁻¹) and still significantly higher than the sediment trap observations. Considerably higher values, around 24–34.5 g C m⁻² yr⁻¹, have been reported from short-term sediment trap deployments in the seasonal ice zone North off Svalbard (Dybwad et al., 2021), being closer to our estimates. Maximum export rates in our simulations of 30–40 mmol C m⁻² d⁻¹ occur 10–20 days before Arctic and Atlantic trajectories reach HAUSGARTEN in the summer setup. For the autumn setup, maxima were higher (ca. 50 mmol C m⁻² d⁻¹) and at a greater temporal distance from the sampling region (50 d for Arctic, 110 d for Atlantic trajectories). These rates are again considerably higher than export rates observed during high carbon export events, which range between 20 and 50 mg C m⁻² d⁻¹ (Cardozo-Mino et al., 2023), that is, 2.4–4.2 mmol C m⁻² d⁻¹.

We note that the apparent overestimation of POC export by our model occurs even though productivity rates and tracer concentrations lay within the ranges we expect from observations, and even though we assume a sinking velocity for detritus of 10 m d⁻¹. Using a larger detritus sinking velocity of 100 m d⁻¹, as is often assumed in the literature (e.g., Bauerfeind et al., 2009; Iversen, 2023), leads to further general overestimation of vertical POC export and underestimation of POC concentrations in the water column during the sampling period, as shown in Figure S6 in Supporting Information S1.

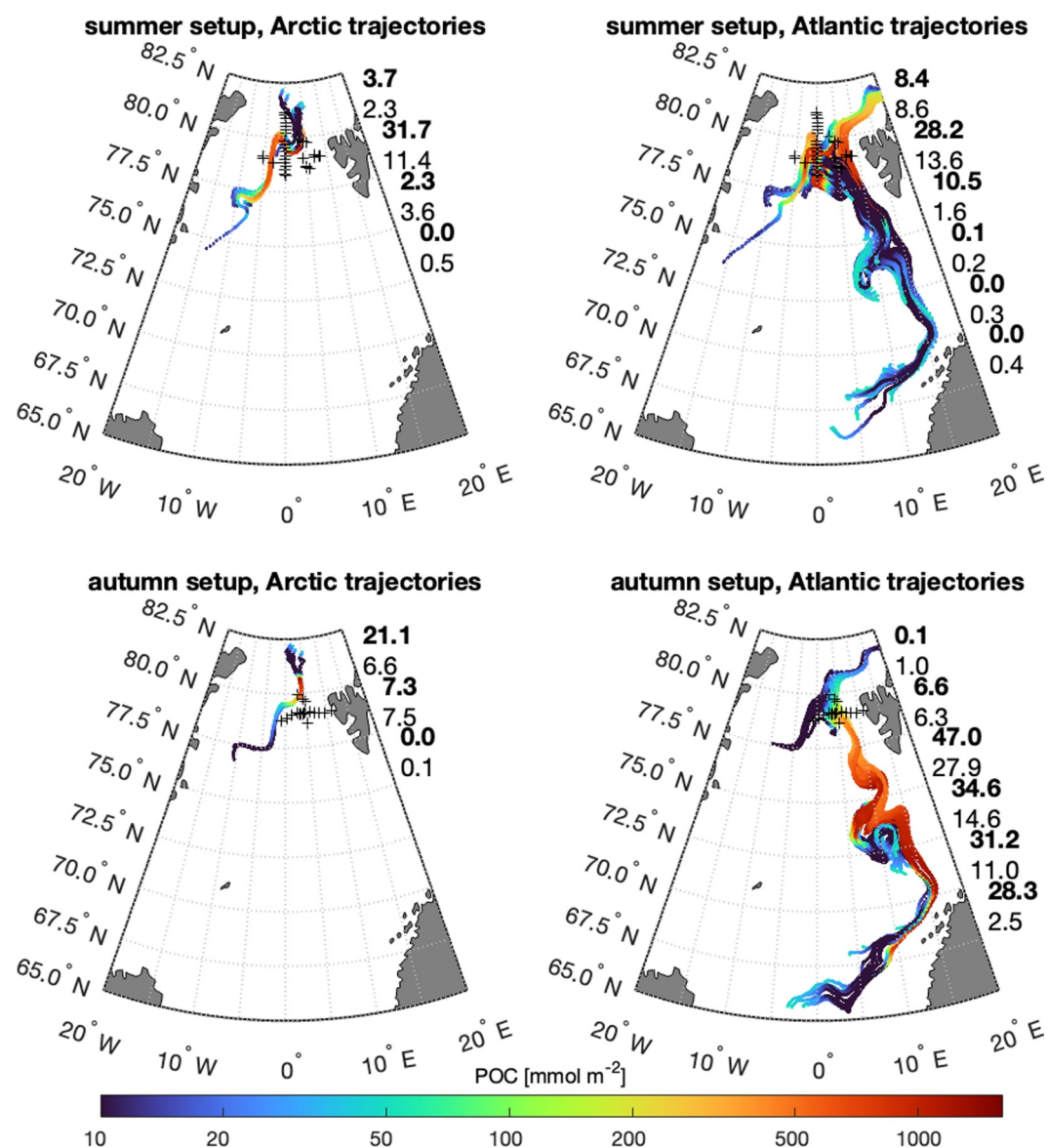


Figure 10. Depth-integrated (100 m) particulate organic carbon concentrations along model trajectories. Numbers in bold font on the right sides represent average Carbon net primary production (integrated over upper 100 m $[\text{mmol C m}^{-2} \text{d}^{-1}]$) fluxes within latitude bins of 2.5°, numbers in regular font represent carbon export at 100 m depth $[\text{mmol C m}^{-2} \text{d}^{-1}]$. In situ sampling locations at HAUSGARTEN are marked with “+” symbols.

4.2. Variations in Plankton Community Structure

The Lagrangian ecosystem model outlined above divides the phytoplankton and zooplankton populations into a number of discrete size-classes, with plankton ecophysiological traits determined by organism size, in line with observed allometric relationships (e.g., Edwards et al., 2012). In line with previous size-structured plankton ecosystem models, our Lagrangian model captures the observed equivalence of phytoplankton biomass in logarithmically-spaced size classes (e.g., Brewin et al., 2014; Schartau et al., 2010). This behavior is a robust feature of size-based marine ecosystem models that include coupled phytoplankton and zooplankton size classes (Ward et al., 2014), and occurs because the biomass within each phytoplankton size class is restricted by top-down grazing pressure from their respective zooplankton predators (Armstrong, 1994).

In situ observations of spring bloom and summer phytoplankton populations in Arctic waters have been described in several publications but are either limited to certain species or limited to specific periods (e.g., Degerlund &

Eilertsen, 2010; Eilertsen et al., 1989; Gradinger & Baumann, 1991; Hasle & Heimdal, 1998; Kubiszyn et al., 2017; Nöthig et al., 2015). In the FS bloom biomass is usually dominated by either colony-forming *Phaeocystis* (0.1–2 mm, Rousseau et al., 2007), also occurring as small flagellates (ca. 2.5 μm), or/and diatom species of the genus *Thalassiosira* (ca. 20 μm) or *Chaetoceros* (ca. 7 μm), accompanied by varying amounts of pennate diatoms (ca. 5–15 μm) such as *Nitzschia*, *Navicula*, and *Fragilariopsis*. Dinoflagellates (ca. 5–20 μm) and other flagellate species (ca. 2–5 μm) are a minor contributing group during spring. In the course of the late summer to autumn a variety of flagellates become more prominent, for instance Hegseth and Sundfjord (2008) found a bloom of *Emiliania huxleyi* (ca. 4–7 μm). In the FS very large cells (up to ca. 180 μm) of the genera *Rhizosolenia* and *Proboscia* were also found during autumn together with small flagellates (Menge, 2019).

Although our model underestimates abundance and biovolume of small—intermediate size classes at times of observations, it resolves the relative shift of biomass from smaller to larger size from summer to autumn that was observed in Lampe et al. (2021). We can link the variability in plankton size structure to bottom-up and top-down controls that have varying effects throughout the productive season, as seen in Figure 11.

Early in the productive season, when nutrient concentrations are high but light availability is low, bottom-up processes dominate. The light limitation term γ_L limits the photosynthetic rate P_j (P_j is the product of the light saturated photosynthetic rate P_j^{sat} and γ_L). This allows for growth of large phytoplankton at low light levels, but only for inefficient growth of small phytoplankton, leading to the pre-bloom peak in phytoplankton size seen in Figure 8. By the beginning of May, when surface irradiance (I^{surf}) exceeds $5 \cdot 10^6 \mu \text{Ein d}^{-1} \text{m}^{-2}$ in the summer setup, the photosynthetic rate reaches 40% (Arctic) to 60% (Atlantic) of P_j^{sat} in larger phytoplankton, but only below 10% in the smallest size class. As the light availability increases, the effects of light limitation decrease. Since the maximum photosynthetic rate P_j^{max} decreases exponentially with cell size, this gradually cancels out the effect of fading size dependent light limitation, allowing rapid growth of small phytoplankton and causing a relative shift of biomass to smaller sizes until the peak of the bloom is reached.

The light saturated photosynthetic rate P_j^{sat} is controlled by a nutrient limitation term $\gamma_{N,j}$, which affects larger cells stronger than smaller cells. However, $\gamma_{N,j}$ never decreases below 0.9, meaning P_j^{sat} is never down-regulated to less than 90% of the maximum photosynthetic rate P_j^{max} due to lack of nutrients. This fits to DIN concentrations in our simulations not falling below 2mmol m^{-3} in the summer setup, never fully exhausting nutrient supply.

Once sufficient zooplankton stocks form, the plankton size structure becomes subject to increasing top-down control through zooplankton grazing. During the bloom, phytoplankton growth occurs in all size classes, but is initially most rapid in the smallest and fastest growing cells. These increasing phytoplankton stocks allow the growth of zooplankton grazers. The grazing pressure is felt most strongly by the smallest phytoplankton, which are preferentially grazed by smaller zooplankton with relatively faster grazing rates (the optimum predator:prey size ratio δ_{opt} is 1:10). The faster response by smaller zooplankton rapidly terminates the growth of smaller phytoplankton populations, causing a relative shift towards larger size classes. As the bloom progresses, the relative size structure shifts towards larger sizes, and zooplankton size follows due to the size-based coupling between predators and prey.

The size structure of the protist planktonic community is an important indicator whether retention or export of accumulated OM is dominant in a system. Communities dominated by large diatoms with silica frustules tend to have high export rates as upon being grazed, they form larger fecal pellets that sink faster (Cael et al., 2021) and are relatively dense and less accessible to microbial degradation (B. Hansen et al., 1996). More recycling as opposed to export is observed in systems that are dominated by picoplankton (Azam et al., 1983). Therefore, unraveling dynamics in the microbial food web is essential to understand mass transfer of OM to higher trophic levels and subsequent recycling or export in the FS.

4.3. Variability in OM Pools

We can link the spatial variability in observed OM pools in the HAUSGARTEN region during summer and autumn to the different Lagrangian pathways (histories) in physical conditions (predominantly light) and ecological dynamics (plankton interaction) each of the simulated trajectories experienced during their voyage.

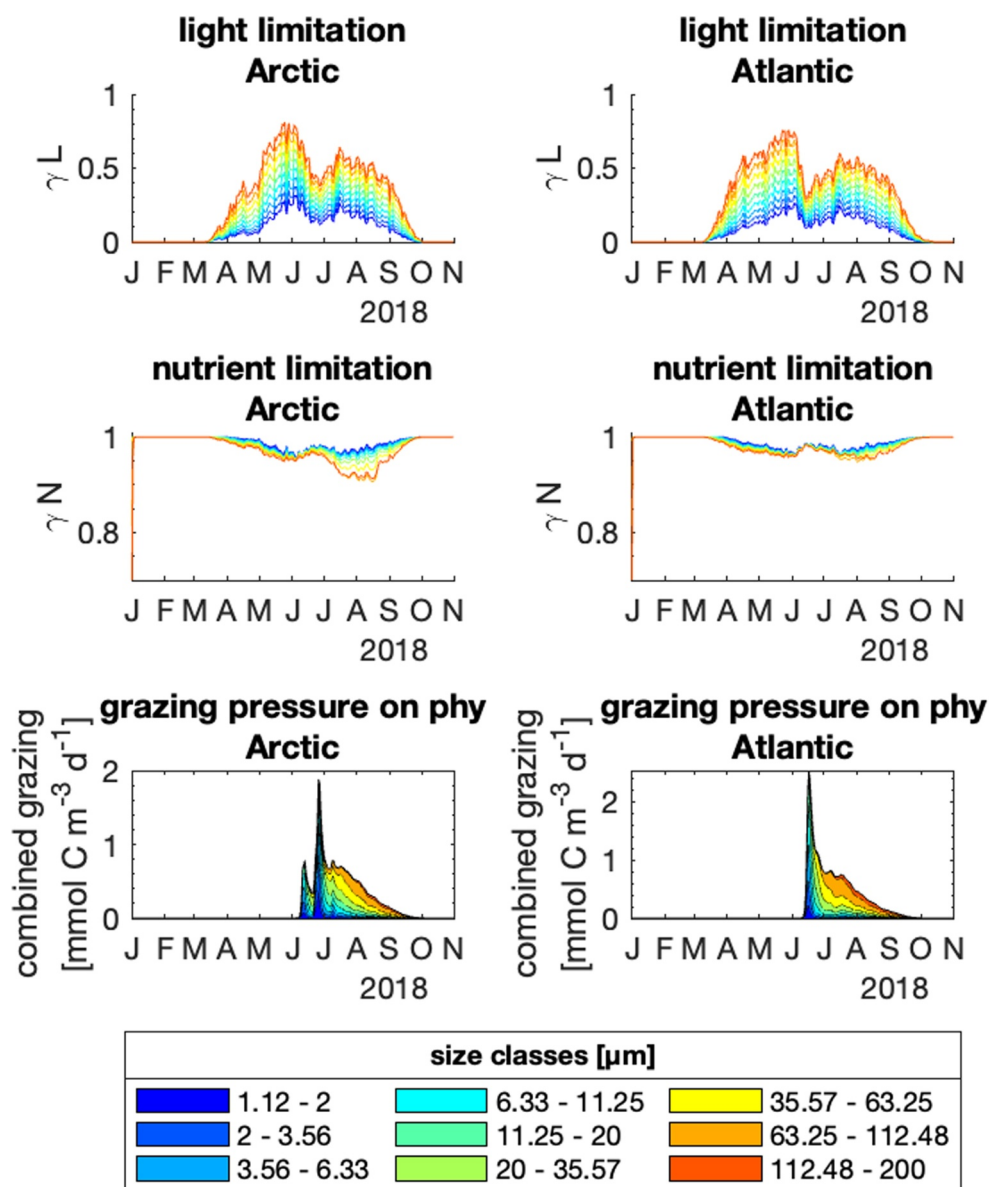


Figure 11. Factors controlling the size composition of phytoplankton stocks in the summer model setup. The photosynthetic rate is limited with a light limitation term γ_L (Equations S8 and S11 in Supporting Information S1). The nutrient limitation term γ_N limits the light saturated photosynthesis rate P_j^{sat} (Equation S7 in Supporting Information S1). Grazing pressure describes the combined grazing of all zooplankton on each phytoplankton size class.

In our model, the partitioning of organic carbon (C_{org}) into living biomass, detritus and DOC is largely controlled by the size structure of the plankton community. Total POC increases in spring until the peak of the bloom, and is mainly made up from phytoplankton biomass. In the following weeks, this leads to an increase in both, detritus and DOC_{SL} . Since the partitioning of C_{org} (generated through background mortality and sloppy feeding) into the dissolved or particulate phase is size dependent (see Equations S25 and S26 in Supporting Information S1), small cells are partitioned roughly 80:20 into DOC:detritus, while the largest 20:80. As the plankton biomass is dominated by smaller size classes during the spring bloom, the DOC to detritus production is at similar levels at this time. With the increase in phytoplankton biomass, zooplankton stocks increase, and their grazing controls phytoplankton stocks. Grazing leads to further increase in detritus (in addition to background mortality), again with a size-dependent partitioning of DOC and detritus. Furthermore, grazing changes the size structure of the plankton, as the smaller plankton are preferentially grazed (the optimal size ratio between predator and prey δ_{opt} is

10:1), which increases carbon allocation into detritus. As a consequence, export of OM increases, since only detritus can be exported via sinking. Compared to the model results, observations in the HAUSGARTEN area for summer and autumn 2018 showed roughly two times higher concentrations for POC but similar ones for DOC_{SL} (Table 2). One process not resolved in the model is the partitioning of DOC into POC due to bacterial uptake and the formation of gel-like particles by aggregation processes, for example, transparent exopolymere particles. TEP contributed on average 1.78 mmol C m⁻³ in summer (von Jackowski et al., 2020a), which would constitute an 25% increase of modeled POC. In autumn TEP-C contributions were lower, that is, 0.59 mmol C m⁻³, equivalent to 30% of modeled POC. Bacterial production drives the microbial food web and is an important sink for DOC (5.47–27.4 g L⁻¹ yr⁻¹).

DOC concentration in the upper 100 m of the water column varies over the productive season in FS and ranged between ca. 40 and 170 μmol L⁻¹ during the period 2009–2017 (Engel et al., 2019). Thereby, the highest concentrations were observed in the upper 20 m, decreasing slightly to 30 m. Considerable variability was still observed at 100 m, ranging between 40 and 95 μmol L⁻¹. Below 250 m, DOC concentration is relatively stable, indicating a refractory pool of 52 ± 2 μmol L⁻¹. Estimates for the production of fresh DOC by Arctic phytoplankton vary around 15% of NPP (Codispoti et al., 2013; Engel et al., 2013). However, variations in the percentage of extracellular release (PER) of photosynthetic carbon may be high, as observed during a study in the Kongsfjord (Svalbard) where PER ranged between 2% and 53% (Engel et al., 2013), or in the Barents Sea where PER was found to vary between 6% and 60% (Vernet et al., 1998). For the Arctic, few measurements of NPP exist; most PP estimates are based on satellite data, where subsurface, marginal or under-ice blooms are not well represented. Primary productivity in June and July 1984, with an average daily integrated productivity of 35 mmol C m⁻² d⁻¹, was also highest at the ice margin in FS during a study by Smith et al. (1987). However, an increase in primary production has been estimated for the pan-Arctic region over the last decades as a consequence of climate change (Ardyna & Arrigo, 2020). Due to the loss of sea ice, the duration of the phytoplankton growing season and the total extent of open water have increased significantly and could explain an estimated 30% increase in NPP between 1998 and 2012, yet largest changes are attributed with ice melting on the shelves (Laptev, Kara, and East Siberian).

4.4. Limitations and Perspectives

The Lagrangian approach allows us to take a different look at the biogeochemical state of a particular region as it is found within a limited period of observations. Even in analyses using three-dimensional coupled physical-biogeochemical ocean models, where the state changes in an area can be resolved in time, supplementary analyses are needed to relate local results to the processes that took place before and outside the region. This is achieved in our study, but is also accompanied by certain disadvantages and limitations.

By using ensembles of trajectories, where a one-dimensional model can be solved in a computationally efficient way, the individual trajectory solutions of the plankton model are independent of each other, even if they are spatially in close proximity to each other. Apart from the identical dynamical equations, the only other connection between some (spatially adjacent) trajectories of an ensemble is the similarity of the physical conditions, since they are based on the same results of a particular circulation model. Horizontal gradients transverse to the trajectories, for example, of Chl-*a*, are not taken into account, while the horizontal mixing and shear remain unresolved, with lateral diffusivities being typically in the order of 10²–10³ m² s⁻¹ (10–10² km² d⁻¹) (e.g., Zhurbas et al., 2014). Lateral mixing may dilute and thus dampen peak concentrations seen in our results, and it likely reduces the variability explained by our approach. In the study of Ser-Giacomi et al. (2023) a Lagrangian approach is proposed where a water patch is subject to strain (changing its shape and size) and diffusion (changing its concentration due to dilution or entrainment of surrounding waters). These explicit considerations provide a more elaborate representation of spatial variability. In principle, such patch dynamics may also be applicable to approaches similar to ours, but it would require additional assumptions with respect to the connectivity, distances and concentration differences, between the individual trajectories.

A distinctive feature of our solutions is that they are all based on an identical set of model parameter values and therefore all differences in the initialization of the bloom are exclusively determined by differences in mixing, light, and temperature conditions imposed as physical forcing. In the case of the Arctic trajectories coming from the north, the model provides a delayed onset of bloom (late May–early June) compared to the remote sensing Chl-*a* data (late April) (Figure 4), while our results are in agreement with the times of bloom initiation in SINMOD

simulations analyzed by Vernet et al. (2021); therein the western FS is referred to as NorthEast (NE) region of Greenland. We note that the bloom detection derived from satellite data is associated with large uncertainties. Although uncertainties in remote sensing in April can be attributed to the low sun angle and the smaller number of pixels that are free of clouds, we think that the delayed onset in our solutions is more likely associated with some dynamics unresolved by the model. Interestingly, the potentially missing mechanisms are also accompanied by a limitation in the visibility of the initial bloom development in the remote sensing data. Ardyna and Arrigo (2020) refer to observations of under-ice phytoplankton blooms (UIBs) that are invisible to remote sensing sensors. Such UIBs, extending from areas fully covered by ice into regions of pack ice, are not accounted for in our model, as well as short-term (diurnal) stratification between the pack ice, which may keep some of the phytoplankton in the upper layers while exposure to light is increased. Another possible, more ecological mechanism that favors earlier bloom development is a reduced grazing pressure on phytoplankton due to increased predation on microzooplankton caused by the seasonal vertical migration of copepods. A model sensitivity analysis of seasonal vertical migration in the southern Labrador Sea (Grossowicz & Pahlow, 2024) revealed that an early ascent of copepods in spring can cause phytoplankton blooms to occur earlier. Such top-down effects can act in combination with the formation of UIBs and the enhancement of algal growth in stratified patches within ice-covered areas, causing bloom development to precede that in the open areas. The mechanisms responsible for the emergence and spread of such blooms appears to be essential, in particular if model applications aim at explaining trends in bloom phenology and NPP in the Arctic, as documented in Lewis et al. (2020) and discussed by Ardyna and Arrigo (2020), in association with the borealisation of Arctic waters, for example, as described by Polyakov et al. (2020).

We would like to emphasize that the mechanisms discussed here, which are not represented by the model, may not be overcome simply by choosing a different set of parameter values for the Arctic trajectories along the marginal ice zone. Although it is possible to improve the match with remote sensing data in the Arctic trajectories, in terms of bloom timing, by adjusting the photosynthetic efficiency (a_p , initial slope of P-I curve), this leads to a misfit in the Chl-*a* depth profile with Chl-*a* maxima now occurring deeper than in observations (Figure S7 in Supporting Information S1).

Considerable improvements might be achieved if the model is further revised with regard to specific size ranges of the grazing, as well as a division of the detritus into fast and slow sinking particles. In this model version of protist plankton, we have only introduced a closure that crudely resolves an impact of higher trophic levels. This is simplistic and if higher trophic levels were explicitly considered, the model solutions would likely change, particularly with respect to the onset of blooms, as discussed above. An implementation of the complex life cycles of copepods, as for example, simulated in Banas, Møller, et al. (2016), goes beyond the scope of our study and would require temporally extended sets of trajectories. To what extent variations in the time of ascent of some vertically migrating copepods can contribute to differences in the overall course of bloom development cannot be evaluated with our model version. In order to elaborate estimates of the ecological effects on primary production and OM export, it could be useful extending the size range of the model accordingly. Finally, apart from the purely ecological effects, we would like to stress that trajectories generated by a model with higher spatial resolution may also serve to increase the simulated variability in the target area.

5. Conclusions

In this study, our primary objective was to unravel the extent to which the spatial variability observed in local measurements of dissolved and particulate OM concentrations, productivity, and export rates in the HAUSGARTEN LTER site could be explained by divergent environmental conditions encountered by water parcels during their transit through the FS. To achieve this, we employed a 1D size-based NPZD plankton ecosystem model with variable stoichiometry, forced by four ensembles of Lagrangian trajectories passing the LTER at different times (summer or autumn) and from distinct directions (originating in the North Atlantic or Arctic Ocean). These trajectories presented diverse sets of physical conditions that plankton within a water parcel may experience along their journey.

Overall, our model has shown that it can generate solutions that are broadly in agreement with data from very different types of observations, comprising tracer concentration measurements, protist plankton spectra derived from microscopy, remote sensing products and climatological data.

Temporal developments in plankton growth, size composition, and OM export varied among trajectory ensembles, despite using identical model parameter values. Light availability discrepancies influenced the timing of

plankton blooms and the size composition of primary producers and thus their grazers, subsequently impacting OM export. During local in situ observations in the FS, maxima in productivity and export had already occurred.

While our model solutions can explain between 10% and 72% of the observed variability, due to the diverse physical conditions of the individual trajectories, a substantial portion of variability remains unexplained. Whether models of higher spatial resolution can overcome such disparities remains unclear, but it certainly underscores the necessity for future research to advance our knowledge of the spatio-temporal variations in plankton dynamics.

Data Availability Statement

The code to generate model simulations and figures can be found on Zenodo (Lampe & Hunter, 2024). In situ data for model calibration are accessible on Pangaea (von Jackowski et al., 2020b; Torres-Valdés et al., 2019). The remote sensing Chl-*a* data were provided through the Ocean Color CCI data product (Sathyendranath et al., 2021). Nutrient concentration data used for model evaluation are available through the World Ocean Atlas (Boyer et al., 2018).

Acknowledgments

We are grateful for the helpful comments of Maria Vernet and an anonymous reviewer that greatly helped us improving this manuscript. We thank Fabian Grosse and Neil Banas for extracting and providing the particle trajectories from SINMOD model results. This paper is an output of microARC, part of the Changing Arctic Ocean Programme. Funding in Germany was provided by the Helmholtz Association and the German Federal Ministry of Education and Research (BMBF: 03F0802A) and in the UK by the UKRI Natural Environment Research Council (NERC: NE/R012822/1). BAW was funded by a Royal Society University Research Fellowship. Open Access funding enabled and organized by Projekt DEAL.

References

- Andersen, K., Berge, T., Gonçalves, R., Hartvig, M., Heuschele, J., Hylander, S., et al. (2016). Characteristic sizes of life in the oceans, from bacteria to Whales. *Annual Review of Marine Science*, 8(1), 217–241. <https://doi.org/10.1146/annurev-marine-122414-034144>
- Ardyna, M., & Arrigo, K. R. (2020). Phytoplankton dynamics in a changing Arctic Ocean. *Nature Climate Change*, 10(10), 892–903. <https://doi.org/10.1038/s41558-020-0905-y>
- Armstrong, R. A. (1994). Grazing limitation and nutrient limitation in marine ecosystems: Steady state solutions of an ecosystem model with multiple food chains. *Limnology & Oceanography*, 39(3), 597–608. <https://doi.org/10.4319/lo.1994.39.3.0597>
- Arrigo, K. R., & Van Dijken, G. L. (2011). Secular trends in Arctic Ocean net primary production. *Journal of Geophysical Research*, 116(C9), C09011. <https://doi.org/10.1029/2011JC007151>
- Azam, F., Fenchel, T., Field, J. G., Gray, J. S., Meyer-Reil, L. A., & Thingstad, F. (1983). The ecological role of water-column microbes in the sea. *Marine Ecology Progress Series*, 10, 257–263. <https://doi.org/10.1021/acs.joc.6b00938>
- Banas, N. S. (2011). Adding complex trophic interactions to a size-spectral plankton model: Emergent diversity patterns and limits on predictability. *Ecological Modelling*, 222(15), 2663–2675. <https://doi.org/10.1016/j.ecolmodel.2011.05.018>
- Banas, N. S. (2018). Particulator [Software]. Retrieved from <https://github.com/neilbanas/particulator>
- Banas, N. S., McDonald, P. S., & Armstrong, D. A. (2009). Green crab Larval retention in Willapa Bay, Washington: An intensive Lagrangian modeling approach. *Estuaries and Coasts*, 32(5), 893–905. <https://doi.org/10.1007/s12237-009-9175-7>
- Banas, N. S., Møller, E. F., Nielsen, T. G., & Eisner, L. B. (2016). Copepod life Strategy and population Viability in response to prey timing and temperature: Testing a new model across latitude, time, and the size spectrum. *Frontiers in Marine Science*, 3, 225. <https://doi.org/10.3389/fmars.2016.00225>
- Banas, N. S., Zhang, J., Campbell, R. G., Sambrotto, R. N., Lomas, M. W., Sherr, E., et al. (2016). Spring plankton dynamics in the Eastern Bering Sea, 1971–2050: Mechanisms of interannual variability diagnosed with a numerical model. *Journal of Geophysical Research: Oceans*, 121(2), 1476–1501. <https://doi.org/10.1002/2015JC011449>
- Barton, A. D., Dutkiewicz, S., Flierl, G., Bragg, J., & Follows, M. J. (2010). Patterns of diversity in marine phytoplankton. *Science*, 327(5972), 1509–1511. <https://doi.org/10.1126/science.1184961>
- Bauerfeind, E., Nöthig, E.-M., Beszczynska, A., Fahl, K., Kaleschke, L., Kreker, K., et al. (2009). Particle sedimentation patterns in the eastern Fram Strait during 2000–2005: Results from the Arctic long-term observatory HAUSGARTEN. *Deep Sea Research Part I: Oceanographic Research Papers*, 56(9), 1471–1487. <https://doi.org/10.1016/j.dsr.2009.04.011>
- Beszczynska-Möller, A., Fahrback, E., Schauer, U., & Hansen, E. (2012). Variability in Atlantic water temperature and transport at the entrance to the Arctic Ocean, 1997–2010. *ICES Journal of Marine Science*, 69(5), 852–863. <https://doi.org/10.1093/icesjms/fss056>
- Błachowiak-Samolyk, K., Wiktor, J. M., Hegseth, E. N., Wold, A., Falk-Petersen, S., & Kubiszyn, A. M. (2015). Winter Tales: The dark side of planktonic life. *Polar Biology*, 38(1), 23–36. <https://doi.org/10.1007/s00300-014-1597-4>
- Blanchard, J. L., Heneghan, R. F., Everett, J. D., Trebilco, R., & Richardson, A. J. (2017). From bacteria to Whales: Using functional size spectra to model marine ecosystems. *Trends in Ecology & Evolution*, 32(3), 174–186. <https://doi.org/10.1016/j.tree.2016.12.003>
- Boyer, T. P., Garcia, H. E., Locarnini, R. A., Zweng, M. M., Mishonov, A. V., Reagan, J. R., et al. (2018). World Ocean Atlas 2018 [Dataset]. NOAA National Centers for Environmental Information. Retrieved from <https://www.ncei.noaa.gov/access/metadata/landing-page/bin/iso?id=gov.noaa.nodc:NCEI-WOA18>
- Brewin, R. J. W., Sathyendranath, S., Tilstone, G., Lange, P. K., & Platt, T. (2014). A multicomponent model of phytoplankton size structure. *Journal of Geophysical Research: Oceans*, 119(6), 3478–3496. <https://doi.org/10.1002/2014JC009859>
- Cael, B. B., Cavan, E. L., & Britten, G. L. (2021). Reconciling the size-dependence of marine particle sinking speed. *Geophysical Research Letters*, 48(5), e2020GL091771. <https://doi.org/10.1029/2020GL091771>
- Cardozo-Mino, M. G., Salter, I., Nöthig, E.-M., Metfies, K., Ramondenc, S., Wekerle, C., et al. (2023). A decade of microbial community dynamics on sinking particles during high carbon export events in the eastern Fram Strait. *Frontiers in Marine Science*, 10, 1173384. <https://doi.org/10.3389/fmars.2023.1173384>
- Codispoti, L., Kelly, V., Thessen, A., Matrai, P., Suttles, S., Hill, V., et al. (2013). Synthesis of primary production in the Arctic Ocean: III. Nitrate and phosphate based estimates of net community production. *Progress in Oceanography*, 110, 126–150. <https://doi.org/10.1016/j.poccean.2012.11.006>
- Comiso, J. C., & Hall, D. K. (2014). Climate trends in the Arctic as observed from space. *Wiley Interdisciplinary Reviews: Climate Change*, 5(3), 389–409. <https://doi.org/10.1002/wcc.277>

- Degerlund, M., & Eilertsen, H. C. (2010). Main species characteristics of phytoplankton spring blooms in NE Atlantic and Arctic waters (68–80° N). *Estuaries and Coasts*, 33(2), 242–269. <https://doi.org/10.1007/s12237-009-9167-7>
- de Steur, L., Hansen, E., Gerdes, R., Karcher, M., Fahrbach, E., & Holfort, J. (2009). Freshwater fluxes in the East Greenland current: A decade of observations. *Geophysical Research Letters*, 36(23), L23611. <https://doi.org/10.1029/2009gl041278>
- Dybwad, C., Assmy, P., Olsen, L. M., Peeken, I., Nikolopoulos, A., Krumpen, T., et al. (2021). Carbon export in the seasonal sea ice zone North of Svalbard from winter to late summer. *Frontiers in Marine Science*, 7, 525800. <https://doi.org/10.3389/fmars.2020.525800>
- Edwards, K. F., Thomas, M. K., Klausmeier, C. A., & Litchman, E. (2012). Allometric scaling and taxonomic variation in nutrient utilization traits and maximum growth rate of phytoplankton. *Limnology & Oceanography*, 57(2), 554–566. <https://doi.org/10.4319/lo.2012.57.2.0554>
- Eilertsen, H., Taasen, J., & Weslawski, J. (1989). Phytoplankton studies in the fjords of West Spitzbergen: Physical environment and production in spring and summer. *Journal of Plankton Research*, 11(6), 1245–1260. <https://doi.org/10.1093/plankt/11.6.1245>
- Engel, A., Borchard, C., Piontek, J., Schulz, K. G., Riebesell, U., & Bellerby, R. (2013). CO₂ increases ¹⁴C primary production in an Arctic plankton community. *Biogeosciences*, 10(3), 1291–1308. <https://doi.org/10.5194/bg-10-1291-2013>
- Engel, A., Bracher, A., Dinter, T., Endres, S., Grosse, J., Metfies, K., et al. (2019). Inter-annual variability of organic carbon concentrations in the eastern Fram Strait during summer (2009–2017). *Frontiers in Marine Science*, 6(April), 187. <https://doi.org/10.3389/fmars.2019.00187>
- Forest, A., Wassmann, P., Slagstad, D., Bauerfeind, E., Nöthig, E.-M., & Klages, M. (2010). Relationships between primary production and vertical particle export at the Atlantic-Arctic boundary (Fram Strait, HAUSGARTEN). *Polar Biology*, 33(12), 1733–1746. <https://doi.org/10.1007/s00300-010-0855-3>
- Garcia, H. E., Weathers, K. W., Paver, C. R., Smolyar, I., Boyer, T. P., Locarnini, R. A., et al. (2019). *World Ocean Atlas 2018. Vol. 4: Dissolved inorganic nutrients (phosphate, nitrate and nitrate+nitrite, silicate) (technical report)*. National Oceanic and Atmospheric Administration.
- Gradinger, R. R., & Baumann, M. E. (1991). Distribution of phytoplankton communities in relation to the large-scale hydrographical regime in the Fram Strait. *Marine Biology*, 111(2), 311–321. <https://doi.org/10.1007/BF01319714>
- Grossowicz, M., & Pahlow, M. (2024). Zooplankton seasonal vertical migration in an optimality-based plankton ecosystem model. *Journal of Plankton Research*, 46(3), 295–306. <https://doi.org/10.1093/plankt/fbae016>
- Hansen, B., Bjørnsen, P. K., & Hansen, P. J. (1994). The size ratio between planktonic predators and their prey. *Limnology & Oceanography*, 39(2), 395–403. <https://doi.org/10.4319/lo.1994.39.2.0395>
- Hansen, B., Fotel, F., Jensen, N., & Madsen, S. (1996). Bacteria associated with a marine planktonic copepod in culture. II. Degradation of fecal pellets produced on a diatom, a nanoflagellate or a dinoflagellate diet. *Journal of Plankton Research*, 18(2), 275–288. <https://doi.org/10.1093/plankt/18.2.275>
- Hansen, E., Gerland, S., Granskog, M. A., Pavlova, O., Renner, A. H. H., Haapala, J., et al. (2013). Thinning of arctic sea ice observed in Fram Strait: 1990–2011: Thinning of arctic sea ice. *Journal of Geophysical Research: Oceans*, 118(10), 5202–5221. <https://doi.org/10.1002/jgrc.20393>
- Hasle, G. R., & Heimdal, B. R. (1998). The net phytoplankton in Kongsfjorden, Svalbard, July 1988, with general remarks on species composition of Arctic phytoplankton. *Polar Research*, 17(1), 31–52. <https://doi.org/10.3402/polar.v17i1.6605>
- Hegseth, E. N., & Sundfjord, A. (2008). Intrusion and blooming of Atlantic phytoplankton species in the high Arctic. *Journal of Marine Systems*, 74(1–2), 108–119. <https://doi.org/10.1016/j.jmarsys.2007.11.011>
- Hibler, W. D. (1979). A dynamic Thermodynamic sea ice model. *Journal of Physical Oceanography*, 9(4), 815–846. [https://doi.org/10.1175/1520-0485\(1979\)0093C0815:ADTSIM3E2.0.CO;2](https://doi.org/10.1175/1520-0485(1979)0093C0815:ADTSIM3E2.0.CO;2)
- Hop, H., Falk-Petersen, S., Svendsen, H., Kwasiński, S., Pavlov, V., Pavlova, O., & Søreide, J. E. (2006). Physical and biological characteristics of the pelagic system across Fram Strait to Kongsfjorden. *Progress in Oceanography*, 71(2–4), 182–231. <https://doi.org/10.1016/j.pocean.2006.09.007>
- Hunke, E. C., & Dukowicz, J. K. (1997). An elastic–viscous–plastic model for sea ice dynamics. *Journal of Physical Oceanography*, 27(9), 1849–1867. [https://doi.org/10.1175/1520-0485\(1997\)027<1849:AEVPMF>2.0.CO;2](https://doi.org/10.1175/1520-0485(1997)027<1849:AEVPMF>2.0.CO;2)
- Iversen, M. H. (2023). Carbon export in the Ocean: A Biologist’s perspective. *Annual Review of Marine Science*, 15(1), 357–381. <https://doi.org/10.1146/annurev-marine-032122-035153>
- Kida, S., & Ito, T. (2017). A Lagrangian view of spring phytoplankton blooms. *Journal of Geophysical Research: Oceans*, 122(11), 9160–9175. <https://doi.org/10.1002/2017JC013383>
- Krause-Jensen, D., & Sand-Jensen, K. (1998). Light attenuation and photosynthesis of aquatic plant communities. *Limnology & Oceanography*, 43(3), 396–407. <https://doi.org/10.4319/lo.1998.43.3.0396>
- Kubiszyn, A., Wiktor, J., Wiktor, J., Jr., Griffiths, C., Kristiansen, S., & Gabrielsen, T. (2017). The annual planktonic protist community structure in an ice-free high Arctic fjord (Adventfjorden, West Spitsbergen). *Journal of Marine Systems*, 169, 61–72. <https://doi.org/10.1016/j.jmarsys.2017.01.013>
- Kuhn, A. M., Dutkiewicz, S., Jahn, O., Clayton, S., Rynearson, T. A., Mazloff, M. R., & Barton, A. D. (2019). Temporal and spatial scales of correlation in marine phytoplankton communities. *Journal of Geophysical Research: Oceans*, 124(12), 9417–9438. <https://doi.org/10.1029/2019JC015331>
- Kuhn, A. M., Mazloff, M., Dutkiewicz, S., Jahn, O., Clayton, S., Rynearson, T., & Barton, A. D. (2023). A global comparison of marine chlorophyll variability observed in Eulerian and Lagrangian perspectives. *Journal of Geophysical Research: Oceans*, 128(7), e2023JC019801. <https://doi.org/10.1029/2023JC019801>
- Lampe, V., & Hunter, A. (2024). Vlampe/microARC: MicroARC model and diagnostics [Dataset]. *Zenodo*. <https://doi.org/10.5281/zenodo.13347803>
- Lampe, V., Nöthig, E.-M., & Schartau, M. (2021). Spatio-temporal variations in community size structure of Arctic protist plankton in the Fram Strait. *Frontiers in Marine Science*, 7, 1–18. <https://doi.org/10.3389/fmars.2020.579880>
- Le Moigne, F. A. C., Poulton, A. J., Henson, S. A., Daniels, C. J., Fragoso, G. M., Mitchell, E., et al. (2015). Carbon export efficiency and phytoplankton community composition in the Atlantic sector of the Arctic Ocean. *Journal of Geophysical Research: Oceans*, 120(6), 3896–3912. <https://doi.org/10.1002/2015JC010700>
- Lévy, M., Jahn, O., Dutkiewicz, S., & Follows, M. J. (2014). Phytoplankton diversity and community structure affected by oceanic dispersal and mesoscale turbulence. *Limnology and Oceanography: Fluids and Environments*, 4(1), 67–84. <https://doi.org/10.1215/21573689-2768549>
- Lewis, K. M., Van Dijken, G. L., & Arrigo, K. R. (2020). Changes in phytoplankton concentration now drive increased Arctic Ocean primary production. *Science*, 369(6500), 198–202. <https://doi.org/10.1126/science.aay8380>
- Litchman, E., Klausmeier, C. A., Schofield, O. M., & Falkowski, P. G. (2007). The role of functional traits and trade-offs in structuring phytoplankton communities: Scaling from cellular to ecosystem level. *Ecology Letters*, 10(12), 1170–1181. <https://doi.org/10.1111/j.1461-0248.2007.01117.x>

- Lorenzen, C. J. (1972). Extinction of light in the Ocean by phytoplankton. *ICES Journal of Marine Science*, *34*(2), 262–267. <https://doi.org/10.1093/icesjms/34.2.262>
- Marañón, E. (2015). Cell size as a Key determinant of phytoplankton Metabolism and community structure. *Annual Review of Marine Science*, *7*(1), 241–264. <https://doi.org/10.1146/annurev-marine-010814-015955>
- Menge, M. (2019). *Sukzession des Phytoplanktons in der östlichen Framstraße - Mikroskopische Auswertung von autonom gesammelten Wasserproben (Bachelor's Thesis)*. Universität Bremen, Alfred-Wegener-Institut für Polar- und Meeresforschung. Retrieved from <https://epic.awi.de/id/eprint/53746/>
- Moloney, C. L., & Field, J. G. (1991). The size-based dynamics of plankton food webs. I. A simulation model of carbon and nitrogen flows. *Journal of Plankton Research*, *13*(5), 1003–1038. <https://doi.org/10.1093/plankt/13.5.1003>
- Nielsen-Englyst, P., Høyer, J. L., Kolbe, W. M., Dybkjær, G., Lavergne, T., Tonboe, R. T., et al. (2023). A combined sea and sea-ice surface temperature climate dataset of the Arctic, 1982–2021. *Remote Sensing of Environment*, *284*, 113331. <https://doi.org/10.1016/j.rse.2022.113331>
- Nöthig, E.-M., Bracher, A., Engel, A., Metfies, K., Niehoff, B., Peeken, I., et al. (2015). Summertime plankton ecology in Fram Strait—A compilation of long- and short-term observations. *Polar Research*, *34*(1), 23349. <https://doi.org/10.3402/polar.v34.23349>
- Nöthig, E.-M., Ramondenc, S., Haas, A., Hehemann, L., Walter, A., Bracher, A., et al. (2020). Summertime in situ chlorophyll a and particulate organic carbon standing stocks in surface waters of the Fram Strait and the Arctic Ocean (1991–2015). *Frontiers in Marine Science*, *7*, 350. <https://doi.org/10.3389/fmars.2020.00350>
- Pelz, M.-T., Schartau, M., Somes, C. J., Lampe, V., & Slawig, T. (2023). A diffusion-based kernel density estimator (diffKDE, version 1) with optimal bandwidth approximation for the analysis of data in geoscience and ecological research. *Geoscientific Model Development*, *16*(22), 6609–6634. <https://doi.org/10.5194/gmd-16-6609-2023>
- Polyakov, I. V., Alkire, M. B., Bluhm, B. A., Brown, K. A., Carmack, E. C., Chierici, M., et al. (2020). Borealization of the Arctic Ocean in response to anomalous advection from Sub-Arctic seas. *Frontiers in Marine Science*, *7*, 491. <https://doi.org/10.3389/fmars.2020.00491>
- Renner, A. H. H., Gerland, S., Haas, C., Spreen, G., Beckers, J. F., Hansen, E., et al. (2014). Evidence of Arctic sea ice thinning from direct observations. *Geophysical Research Letters*, *41*(14), 5029–5036. <https://doi.org/10.1002/2014GL060369>
- Rousseau, V., Chrétiennot-Dinet, M. J., Jacobsen, A., Verity, P., & Whipple, S. (2007). The life cycle of Phaeocystis: State of knowledge and presumptive role in ecology. *Biogeochemistry*, *83*(1–3), 29–47. <https://doi.org/10.1007/s10533-007-9085-3>
- Salter, I., Bauerfeind, E., Fahl, K., Iversen, M. H., Lalande, C., Ramondenc, S., et al. (2023). Interannual variability (2000–2013) of mesopelagic and bathypelagic particle fluxes in relation to variable sea ice cover in the eastern Fram Strait. *Frontiers in Earth Science*, *11*, 1210213. <https://doi.org/10.3389/feart.2023.1210213>
- Sathyendranath, S., Jackson, T., Brockmann, C., Brotas, V., Calton, B., Chuprin, A., et al. (2021). ESA ocean colour climate change initiative (Ocean_Colour_cci): Version 5.0 data [Dataset]. *NERC EDS Centre for Environmental Data Analysis*. <https://doi.org/10.5285/1dbe7a109c0244aad713e078fd3059a>
- Schartau, M., Landry, M. R., & Armstrong, R. A. (2010). Density estimation of plankton size spectra: A reanalysis of IronEx II data. *Journal of Plankton Research*, *32*(8), 1167–1184. <https://doi.org/10.1093/plankt/fbq072>
- Ser-Giacomi, E., Martinez-Garcia, R., Dutkiewicz, S., & Follows, M. J. (2023). A Lagrangian model for drifting ecosystems reveals heterogeneity-driven enhancement of marine plankton blooms. *Nature Communications*, *14*(1), 6092. <https://doi.org/10.1038/s41467-023-41469-2>
- Serra-Pompei, C., Ward, B. A., Pinti, J., Visser, A. W., Kjørboe, T., & Andersen, K. H. (2022). Linking plankton size spectra and community composition to carbon export and its efficiency. *Global Biogeochemical Cycles*, *36*(5), e2021GB007275. <https://doi.org/10.1029/2021GB007275>
- Slagstad, D., & McClimans, T. A. (2005). Modeling the ecosystem dynamics of the Barents Sea including the marginal ice zone: I. Physical and chemical oceanography. *Journal of Marine Systems*, *58*(1–2), 1–18. <https://doi.org/10.1016/j.jmarsys.2005.05.005>
- Slagstad, D., Wassmann, P. F. J., & Ellingsen, I. (2015). Physical constrains and productivity in the future Arctic Ocean. *Frontiers in Marine Science*, *2*, 85. <https://doi.org/10.3389/fmars.2015.00085>
- Smith, W. O., Baumann, M. M. E., Wilson, D. L., & Aletsee, L. (1987). Phytoplankton biomass and productivity in the marginal ice zone of the Fram Strait during summer 1984. *Journal of Geophysical Research*, *92*(C7), 6777–6786. <https://doi.org/10.1029/jc092ic07p06777>
- Soltwedel, T., Bauerfeind, E., Bergmann, M., Bracher, A., Budaeva, N., Busch, K., et al. (2016). Natural variability or anthropogenically-induced variation? Insights from 15 years of multidisciplinary observations at the arctic marine LTER site HAUSGARTEN. *Ecological Indicators*, *65*, 89–102. <https://doi.org/10.1016/j.ecolind.2015.10.001>
- Soltwedel, T., Bauerfeind, E., Bergmann, M., Budaeva, N., Hoste, E., Jaeckisch, N., et al. (2005). Hausgarten: Multidisciplinary investigations at a Deep-sea, long-term observatory in the Arctic Ocean. *Oceanography*, *18*(3), 46–61. <https://doi.org/10.5670/oceanog.2005.24>
- Spreen, G., De Steur, L., Divine, D., Gerland, S., Hansen, E., & Kwok, R. (2020). Arctic Sea ice volume export through Fram Strait from 1992 to 2014. *Journal of Geophysical Research: Oceans*, *125*(6), e2019JC016039. <https://doi.org/10.1029/2019JC016039>
- Stroeve, J. C., Serreze, M. C., Holland, M. M., Kay, J. E., Malanik, J., & Barrett, A. P. (2012). The Arctic's rapidly shrinking sea ice cover: A research synthesis. *Climatic Change*, *110*(3–4), 1005–1027. <https://doi.org/10.1007/s10584-011-0101-1>
- Sundfjord, A., Ellingsen, I., Slagstad, D., & Svendsen, H. (2008). Vertical mixing in the marginal ice zone of the northern Barents Sea—Results from numerical model experiments. *Deep Sea Research Part II: Topical Studies in Oceanography*, *55*(20–21), 2154–2168. <https://doi.org/10.1016/j.dsr2.2008.05.027>
- Thorarindottir, T. L., Gneiting, T., & Gissibl, N. (2013). Using proper divergence functions to evaluate climate models. *SIAM/ASA Journal on Uncertainty Quantification*, *1*(1), 522–534. <https://doi.org/10.1137/130907550>
- Torres-Valdés, S., Morische, A., & Wischniewski, L. (2019). Nutrient measurements from POLARSTERN cruise PS114 (LTER HAUSGARTEN) [Dataset]. *PANGAEA*. <https://doi.org/10.1594/PANGAEA.907355>
- Vernet, M., Ellingsen, I., Marchese, C., Bélanger, S., Cape, M., Slagstad, D., & Matrai, P. A. (2021). Spatial variability in rates of net primary production (NPP) and onset of the spring bloom in Greenland shelf waters. *Progress in Oceanography*, *198*, 102655. <https://doi.org/10.1016/j.pocean.2021.102655>
- Vernet, M., Matrai, P. A., & Andreassen, I. (1998). Synthesis of particulate and extracellular carbon by phytoplankton at the marginal ice zone in the Barents Sea. *Journal of Geophysical Research*, *103*(C1), 1023–1037. <https://doi.org/10.1029/97JC02288>
- von Jackowski, A., Becker, K. W., Wietz, M., Bienhold, C., Zäncker, B., Nöthig, E. M., & Engel, A. (2022). Variations of microbial communities and substrate regimes in the eastern Fram Strait between summer and fall. *Environmental Microbiology*, *24*(9), 4124–4136. <https://doi.org/10.1111/1462-2920.16036>
- von Jackowski, A., Grosse, J., Nöthig, E. M., & Engel, A. (2020a). Dynamics of organic matter and bacterial activity in the Fram Strait during summer and autumn. *Philosophical transactions. Series A, Mathematical, physical, and engineering sciences*, *378*(2181), 20190366. <https://doi.org/10.1098/rsta.2019.0366>

- von Jackowski, A., Grosse, J., Nöthig, E.-M., & Engel, A. (2020b). Organic matter and bacteria measurements of POLARSTERN cruise PS114 and Maria S. Merian cruise MSM77 [Dataset]. *PANGAEA*. <https://doi.org/10.1594/PANGAEA.915751>
- Ward, B. A., Dutkiewicz, S., & Follows, M. J. (2014). Modelling spatial and temporal patterns in size-structured marine plankton communities: Top-down and bottom-up controls. *Journal of Plankton Research*, *36*(1), 31–47. <https://doi.org/10.1093/plankt/ftb097>
- Ward, B. A., Dutkiewicz, S., Jahn, O., & Follows, M. J. (2012). A size-structured food-web model for the global ocean. *Limnology & Oceanography*, *57*(6), 1877–1891. <https://doi.org/10.4319/lo.2012.57.6.1877>
- Ward, B. A., & Follows, M. J. (2016). Marine mixotrophy increases trophic transfer efficiency, mean organism size, and vertical carbon flux. *Proceedings of the National Academy of Sciences of the United States of America*, *113*(11), 2958–2963. <https://doi.org/10.1073/pnas.1517118113>
- Ward, B. A., Marañón, E., Sauterey, B., Rault, J., & Claessen, D. (2017). The size dependence of phytoplankton growth rates: A trade-off between nutrient uptake and Metabolism. *The American Naturalist*, *189*(2), 170–177. <https://doi.org/10.1086/689992>
- Wassmann, P., Slagstad, D., & Ellingsen, I. (2010). Primary production and climatic variability in the European sector of the Arctic Ocean prior to 2007: Preliminary results. *Polar Biology*, *33*(12), 1641–1650. <https://doi.org/10.1007/s00300-010-0839-3>
- Wassmann, P., Slagstad, D., Riser, C. W., & Reigstad, M. (2006). Modelling the ecosystem dynamics of the Barents Sea including the marginal ice zone: II. Carbon flux and interannual variability. *Journal of Marine Systems*, *59*(1–2), 1–24. <https://doi.org/10.1016/j.jmarsys.2005.05.006>
- Wekerle, C., Hattermann, T., Wang, Q., Crews, L., Von Appen, W.-J., & Danilov, S. (2020). Properties and dynamics of mesoscale eddies in Fram Strait from a comparison between two high-resolution ocean–sea ice models. *Ocean Science*, *16*(5), 1225–1246. <https://doi.org/10.5194/os-16-1225-2020>
- Wietz, M., Bienhold, C., Metfies, K., Torres-Valdés, S., von Appen, W.-J., Salter, I., & Boetius, A. (2021). The polar night shift: Seasonal dynamics and drivers of Arctic Ocean microbiomes revealed by autonomous sampling. *ISME Communications*, *1*(1), 76. <https://doi.org/10.1038/s43705-021-00074-4>
- Zhurbas, V., Lyzhkov, D., & Kuzmina, N. (2014). Drifter-derived estimates of lateral eddy diffusivity in the world ocean with emphasis on the Indian Ocean and problems of parameterisation. *Deep Sea Research Part I: Oceanographic Research Papers*, *83*, 1–11. <https://doi.org/10.1016/j.dsr.2013.09.001>

Erratum

The originally published version of this article contained typographical errors in Equations 7 and 8. In Equation 7, the minus sign should precede “WOA.” In equation 8, the minus sign should precede the “(s)” in both places in the equation. In addition, in the eleventh sentence of the second paragraph of Section 4.3, “mmol C L⁻³” should be changed to “mmol C m⁻³.” In Table 1, mathematical expressions in the following rows of the column labeled “(#) Notation” were incorrectly formatted: row 10, row 14, and row 17. Mathematical expressions in rows 18–24 of the column labeled “Values” were incorrectly formatted. In Table 2, mathematical expressions were incorrectly formatted in the seventh and eighth column headings and the first and second sentences of the table note. The mathematical expression in the second sentence of the caption for Figure 2 was incorrectly formatted. Mathematical expressions were incorrectly formatted in the following locations of the main text: the tenth, eleventh and twelfth sentences of the first paragraph of Section 2.2.1, the first sentence of the fourth paragraph of Section 2.2.2, the fifth sentence of the second paragraph of Section 2.4, the third sentence of the first paragraph of Section 3.2.2, the fourth and fifth sentences of the second paragraph of Section 3.2.2, the first sentence of the third paragraph of Section 3.2.2, the first and third sentences of the fourth paragraph of Section 3.2.2, the second sentence of the third paragraph of Section 4.2, and the first, third, fourth, and tenth sentences of the second paragraph of Section 4.3. The errors have been corrected, and this may be considered the authoritative version of record.